



MASTER'S THESIS  
45 ECTS

# Circumstellar Dust Shells around Evolved Massive Stars

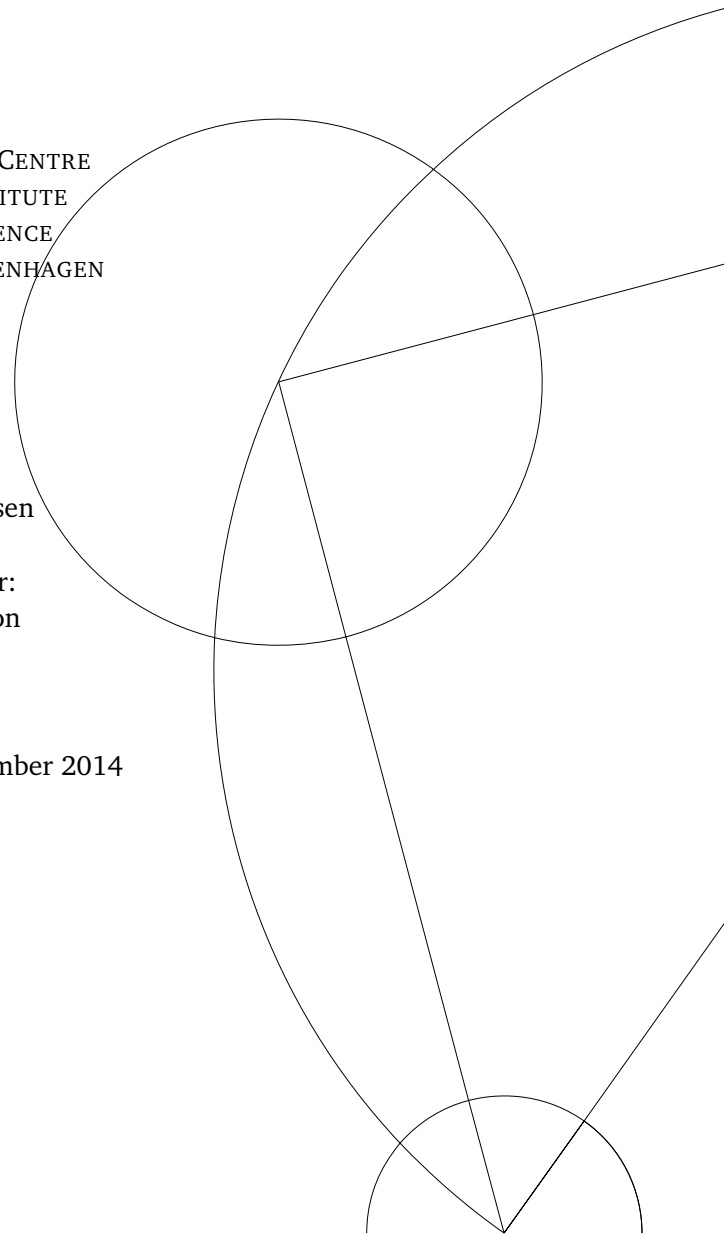
Sarah Massalkhi

DARK COSMOLOGY CENTRE  
NIELS BOHR INSTITUTE  
FACULTY OF SCIENCE  
UNIVERSITY OF COPENHAGEN

Supervisor:  
Anja C. Andersen

Co-supervisor:  
Darach Watson

Submitted: 8<sup>th</sup> September 2014





### **Abstract**

This project focuses on estimating the temperatures and masses of ejected circumstellar dust shells using a sample of evolved massive stars. Aperture photometry was performed on the sample at mid- and far-infrared wavelengths. The measured flux densities were fitted by a modified blackbody which accounts for an emissivity spectral index,  $\beta$ . The latter is influenced by the properties of dust grains, such as grain size and composition. In this thesis, three different values of  $\beta = 1, 1.5$  and  $2$  were investigated. The best-fit dust temperatures were found and used to estimate the masses of the ejected dust. Moreover, three different dust compositions were explored when estimating the masses. I conclude that the dust temperatures are influenced by the properties of dust grains. In addition, the dust masses are revealed dependency on the composition of the grains. The derived dust masses infer low-mass nebulae ejected by these type of stars.



# Acknowledgments

Six months ago I started this thesis, and it turned out to be a long battle with a few stars that may or may not even exist today. This is the result of long days spent at the office, the joy of good results, the sadness and frustration with each failed attempt.

One stick of bamboo cannot make a raft, and a solo effort cannot make a thesis. I owe many people my deepest appreciation for the completion of this thesis.

My heart-felt gratitude goes to my mom, dad, my brother and sister for the unconditional love and support. None of this would have been possible with your continuous understanding, encouragement and above all, belief in me.

I would like to thank my supervisor Anja Anderson for taking me under her wings as a Master's student, for the unending support, for the guidance, and for the inspiration that always ignited a spark in me. My co-supervisor Darach Watson for the wealthy knowledge and assistance and Julie Wardlow for her patience and kindness. Thank you for the smiles no matter how many times I came knocking on your door.

I would like to say a thousand thanks to my close friend, Roy Aad, who was a great support during these two years even when miles were in between.

To the staff at DARK, and my office mates for being so friendly and welcoming. Working at the office wouldn't have been the same without you.

To the great people I befriended since I came to Denmark. Svavar, thank you for the movie nights, the piano melodies, and discussions, whether it is about the Norse mythology, or Donkey Kong tricks.

To Birgit, who has been the grandma figure I never had.

To my dearest friends in Lebanon.

To my momentary sources of inspiration that paved the way for numerous artistic outbursts. I owe you a very profound gratitude.

And now I await the defense that should wrap up this journey!



*And the rest is rust and stardust.*

VLADIMIR NABOKOV



# Contents

<b>1</b>	<b>Introduction</b>	<b>5</b>
1.1	Stars and Their Environment . . . . .	5
1.1.1	Motivation and Project Description . . . . .	7
1.2	The Infrared Eyes . . . . .	8
1.2.1	The Herschel Space Observatory . . . . .	8
1.2.2	The Spitzer Space Telescope . . . . .	10
1.3	The Life of Stars - a Brief Review . . . . .	12
1.3.1	Formation and Evolution . . . . .	12
1.4	Stellar Winds . . . . .	16
1.5	Dust Emission . . . . .	17
1.6	The Spectral Energy Distribution of Dust . . . . .	19
1.7	Estimating the Dust Mass . . . . .	20
<b>2</b>	<b>Theory</b>	<b>24</b>
2.1	Cosmic Dust from Massive Stars . . . . .	24
2.2	Circumstellar Material around Different Types of Evolved Massive Stars . . . . .	25
2.3	Detection Methods . . . . .	32
<b>3</b>	<b>Data Analysis</b>	<b>34</b>
3.1	Computational Tools . . . . .	35
3.1.1	SAOImage DS9 . . . . .	35
3.1.2	HIPE . . . . .	36
3.1.3	Aperture Photometry Tool . . . . .	37
3.2	<i>Spitzer Maps</i> . . . . .	38
3.3	<i>Herschel Maps</i> . . . . .	39
3.4	Selection of Sample . . . . .	40
3.5	Contours and RGB Images . . . . .	40
3.6	Source Detection and Photometry . . . . .	41
3.6.1	Image Units Conversion . . . . .	41
3.6.2	MIPS-24 $\mu\text{m}$ and PACS-70 $\mu\text{m}$ Aperture Photometry . . . . .	43
3.6.3	PACS-160 $\mu\text{m}$ and SPIRE-250 $\mu\text{m}$ Aperture Photometry . . . . .	45
<b>4</b>	<b>Results and Discussion</b>	<b>54</b>
4.1	Dust Temperature . . . . .	54

CONTENTS 4

---

4.2 Dust Mass . . . . .	58
<b>5 Summary and Conclusion</b>	<b>65</b>
<b>A Contoured and RGB Images</b>	<b>68</b>
<b>B The Objects</b>	<b>77</b>

# Chapter 1

## Introduction

### 1.1 Stars and Their Environment

Our universe contains a wide array of celestial objects such as stars, planets, moons, asteroids, comets, nebulae, galaxies, pulsars, quasars, and blackholes. All are surrounded by the interstellar medium that fills the space between these astronomical objects. These regions mainly consist of gas (99%) and dust (1%) (Boulanger et al. (2000)).

The interstellar dust is made of extremely small particles comparable to the blue light wavelength (few microns in radius) with irregular shapes and are generally thought to be composed of water ice, graphite, silicates and their compounds (Draine (2003)).

Thick regions of dust can block light passing through them resulting in dark clouds, known as dark nebulae. Dust can absorb and can attenuate the light passing through it by scattering it away from the line of sight. The combination between *scattering* and *absorption* is known as *extinction*. Dust particles can also cause *interstellar reddening*. Since the size of the dust particles strongly scatter shorter wavelengths (blue light), longer wavelengths (red light) pass unhindered, making objects appear dimmer and redder (Karttunen et al. (2007)).

The interstellar gas is made up of 75% hydrogen and the remaining 25% of helium. Part of the interstellar gas consists of neutral atoms and molecules and the other part charged particles. The interstellar gas typically exists in the form of two states: a cold state consisting of clouds of neutral, either atomic or molecular hydrogen (HI region) and a hot state where the hydrogen is ionized from nearby star-forming regions (HII region).

HII regions are very crucial to star formation processes. Stars form in cold dense giant molecular clouds. The stars emit winds and ultraviolet (UV) radiation which ionizes the hydrogen and creates a cavity in the surrounding molecular cloud allowing the hot ionized gas of the HII region to expand into it. When the gas from the HII region encounters the gas from the molecular cloud, a shock wave is produced compressing the gas in the molecular cloud. The resulting high temperatures and pressures marks a period of concentrated star formation where clusters of stars arise. These in return ionize the HII region and the same process is repeated.

During their lives, stars don't preserve the same mass from their birth to their death but instead lose a fraction of it to the interstellar medium via stellar winds. This mass loss is heightened during the end of the evolution of massive stars in particular. Due to the nuclear processes that take place inside the stars, this material injected often contributes to the enrichment of the interstellar medium. The ejection of mass into the surrounding of the star is accompanied by injection of momentum and energy as well. This causes fluctuations in the interstellar medium which act as seeds for the formation of a new generation of stars and galaxies (Kwok (2007)).

The interaction between the stellar wind and the interstellar medium results in various astronomical phenomena such as wind bubbles and circumstellar nebulae around massive stars. Massive stars are stars that are born with a mass eight times greater than that of the Sun and that can amass more than 100 times of it (1 solar mass,  $M_{\odot}$ , is the mass of the Sun,  $1.981 \times 10^{30}$  kgs). These stars live short and die hard. Nearing the end of their lives, massive stars lose a substantial fraction of their mass to their surrounding medium in the form of copious stellar winds before detonating as supernovae (Lamers and Cassinelli (1999)). These structures surround their central stars and are not gravitationally bound to them and are made of the outer material of their progenitors.

## 1.1.1 Motivation and Project Description

The characteristics of circumstellar nebulae, from morphology, to mass, to luminosity, are highly dependent on the amounts of material expelled by the star. This is one of the main reasons why these circumstellar nebulae are of intriguing interest; they hold a valuable record of the mass loss of their progenitors. Investigating their observational physical properties such as mass, expansion, composition, and morphology to name a few, has the optimum potential to give insight into the evolution of the stars, and can be useful in improving our understanding of the properties of massive stars.

The Spitzer Space Telescope recently discovered a population of hidden circumstellar shells around massive stars. The results are described in details in two papers (Gvaramadze et al. (2010), Wachter et al. (2010)) which this thesis is inspired from and based upon.

The aim of this project is to eventually estimate the dust mass ejected from five evolved massive stars presented in the papers mentioned above. This was done by carrying out photometric analysis of the emission of these dust shells around the massive stars at the mid-infrared wavelengths,  $24\ \mu\text{m}$ , observed by *Spitzer*, as well as their corresponding far-infrared wavelengths,  $70\ \mu\text{m}$ ,  $160\ \mu\text{m}$  and  $250\ \mu\text{m}$  observed by the Herschel Space Observatory. The photometric analysis yielded flux densities of the dust emission at their observed wavelengths, and were then fitted with modified blackbodies under certain assumptions further explained throughout the course of this thesis. The derived dust temperatures from the fitting were used to equivalently estimate the mass of the material ejected by the evolved massive stars.

In the section to follow, I briefly introduce the Spitzer Space Telescope and the Herschel Space Observatory which have presented the astronomical community with unparalleled information about the infrared sky due to both, their resolution and sensitivity, revealing a wealth of information about the dim, faint, and faraway.

## 1.2 The Infrared Eyes

While the visible spectrum allows direct detection of starlight and basic emission lines, other features of the universe, which do not emit considerable visible light to be detected directly, require other means of observation using wavelengths other than the visible.

Approximately half of the UV radiation absorbed by the dust is re-emitted as infrared (IR) radiation (Hauser and Dwek (2001), Dole et al. (2006), Dale et al. (2007)). Observing in the near IR ( $0.7\text{--}5\ \mu\text{m}$ ) allows the detection of cool stars emission ( $740\text{--}5200\ \text{K}$ ) such as red giants and cooler red stars, where dust in this case is transparent to these wavelengths. Going into the mid-IR ( $5\text{--}40\ \mu\text{m}$ ), the thermal emission from dust itself becomes observable and one is able to detect warm dust ( $92\text{--}740\ \text{K}$ ) heated by starlight. Going further into the far-IR ( $40\text{--}350\ \mu\text{m}$ ) one is able to detect the emission from cold dust and very cold clouds ( $11\text{--}39\ \text{K}$ ). The Spitzer Space Telescope was designed to detect at mid- and far-IR wavelengths covering a range of ( $3\text{--}160\ \mu\text{m}$ ) and the Herschel Space Observatory was designed to detect far-IR and submillimeter (sub-mm) wavelengths covering a range of ( $60\text{--}670\ \mu\text{m}$ ).

### 1.2.1 The Herschel Space Observatory

The Herschel Space Observatory built and run by the *European Space Agency* was designed to detect radiation at far-IR and sub-mm wavelengths allowing it to observe cold, distant and obscured objects in the universe. *Herschel* was launched in May 2009 and ended its mission in April 2013. It was located at a point in space about 1.5 million kms away from Earth in an opposite direction of the Sun to avoid as much radiation as possible that would heat the telescope. It did not orbit the Earth in the widely known conventional manner of most satellites, instead it orbited around the second Lagrangian point of the Sun-Earth system (or 'L2'). With a primary mirror 3.5-meter in diameter, it is the largest space telescope ever built. On board of *Herschel* were three instruments called PACS, HIFI and SPIRE which capabilities involved photometry and spectroscopy in the full 55-672 micron range.

A brief overview on each instrument:

- **PACS: The Photodetector Array Camera and Spectrometer** functioned as either a photometer or a low-resolution spectrometer over a wavelength range of  $\sim 60\text{--}210\ \mu\text{m}$  with the camera operating in three different bands centered at  $70\ \mu\text{m}$ ,  $100\ \mu\text{m}$ , and  $160\ \mu\text{m}$  taking images simultane-



Figure 1.1: The Herschel Space Observatory. credit: National Astronomical Observatories (2012)

ously in two bands, the first always fixed and centered at  $160\ \mu\text{m}$  while the second can be selected either at  $70\ \mu\text{m}$  or  $100\ \mu\text{m}$ . It covered a field of view of  $1.75 \times 3.5$  arcminutes (camera) and  $50 \times 50$  arcseconds (spectrometer) with a resolution of 5 arcseconds (camera), and 10 arcseconds (spectrometer). Its sensitivity, or point source detection limit was  $\sim 5$  mJy at  $70\ \mu\text{m}$  and  $100\ \mu\text{m}$  and  $\sim 10$  mJy (millijanskys) at  $160\ \mu\text{m}$ . For further info, see Poglitsch et al. (2010) and Manual (2011).

- **HIFI: The Heterodyne Instrument for the Far Infrared** functioned as a spectrometer that was sensitive to  $\sim 157 - 625\ \mu\text{m}$ . It was not an imaging instrument, and it observed the sky one pixel at a time. For further info, see De Graauw et al. (2010).

- **SPIRE:** The **Spectral and Photometric Imaging REceiver**, like PACS, also functioned as either a photometer or a low-resolution spectrometer over a wavelength range of  $\sim 200\text{--}670$ . The photometer camera took images simultaneously at three bands centered at  $250\ \mu\text{m}$ ,  $350\ \mu\text{m}$ , and  $500\ \mu\text{m}$ . It was able to detect point sources with brightness above 2 mJy for point sources and between 4 and 9 mJy for extended sources. The spectrometer was able to image point sources with brightnesses  $\sim 100$  millijanskys (mJy) and extended sources with brightnesses of  $\sim 500\text{mJy}$ . SPIRE covered a field of view of  $4 \times 8$  arcminutes (camera) and  $2.6 \times 2.6$  arcseconds (spectrometer) with a resolution of  $20\text{--}30$  arcseconds (camera), and  $20\text{--}50$  arcseconds (spectrometer). For further info, see Griffin et al. (2010).

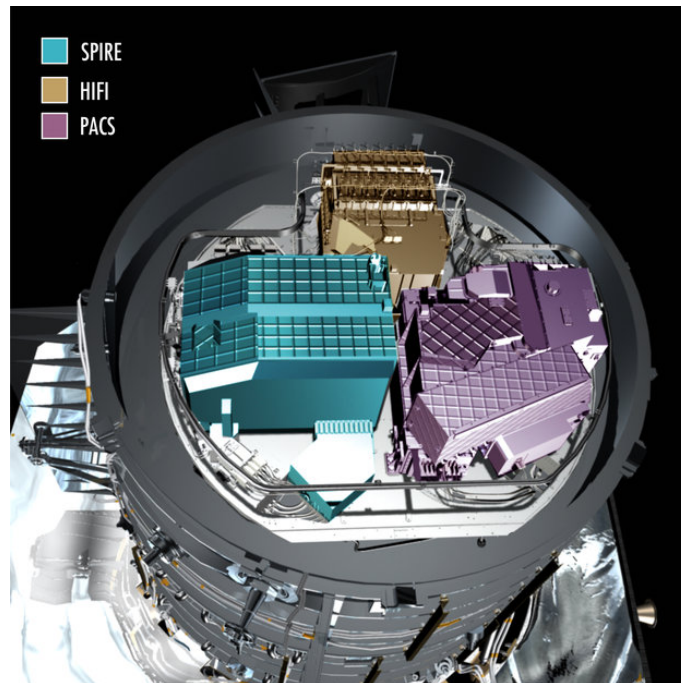


Figure 1.2: PACS, SPIRE, and HIFI on board of *Herschel*. credit:esa (2007)

## 1.2.2 The Spitzer Space Telescope

The Spitzer Space Telescope was launched in August 2003 in a heliocentric orbit around the Earth. It was a part of NASA's Great Observatories Program. *Spitzer* observes the universe in the IR regime covering a range from  $3.6$  to  $180\ \mu\text{m}$ . On board of *Spitzer* are three instruments: MIPS, IRAC and IRS. For detailed information about the instruments, see Rieke et al. (2004).

A brief overview on each instrument:

- **MIPS** The **Multiband Imaging Photometer** operates as a deep imaging camera in the far-IR regime at wavelengths  $24\mu\text{m}$ ,  $70\mu\text{m}$  and  $160\mu\text{m}$  and is also capable of simple spectroscopy between  $52\mu\text{m}$  and  $100\mu\text{m}$ . The  $24\mu\text{m}$  band is a  $128 \times 128$  arsenic-doped silicon (Si:As) array. It has a field of view of 5 arcmin. The  $70\mu\text{m}$  band is a  $32 \times 32$  gallium-doped germanium (Ge:Ga) array with a 5 arcmin field of view. The  $160\mu\text{m}$  is a  $2 \times 20$  Ge:Ga array with  $0.5 \times 5$  arcmin field of view.
- **IRAC** The **Infrared Array Camera** detects lights at the near- and mid-IR wavelengths covering a range between  $3\mu\text{m}$  and  $8\mu\text{m}$  centered at 3.6, 4.5, 5.8 and  $8\mu\text{m}$ . Each detector array is  $256 \times 256$  pixels in size covering a  $5.12 \times 5.12$  arcmin field of view. The images are later turned into mosaics. In the short wavelength a pair (3.6 and  $4.5\mu\text{m}$ ) of indium antimonide (InSb) detectors are used while in the long wavelength ( $5.8$  and  $8\mu\text{m}$ ), a arsenic-doped silicon detector is used (Si:As IBC).
- **IRS** The **Infrared Spectrograph** operates as a low- and high-spectrograph at mid-IR wavelengths, from 5 to  $40\mu\text{m}$ ). A low-resolution module operates between  $5.3$  and  $14\mu\text{m}$ , a short wavelength high-resolution module between 10 and  $19.5\mu\text{m}$ , and a long wavelength high-resolution module at 19 to  $37\mu\text{m}$ . The detector arrays have sizes of  $128 \times 128$  pixels. The short wavelength detectors are treated with arsenic, and long wavelength silicon detectors are treated with antimony.

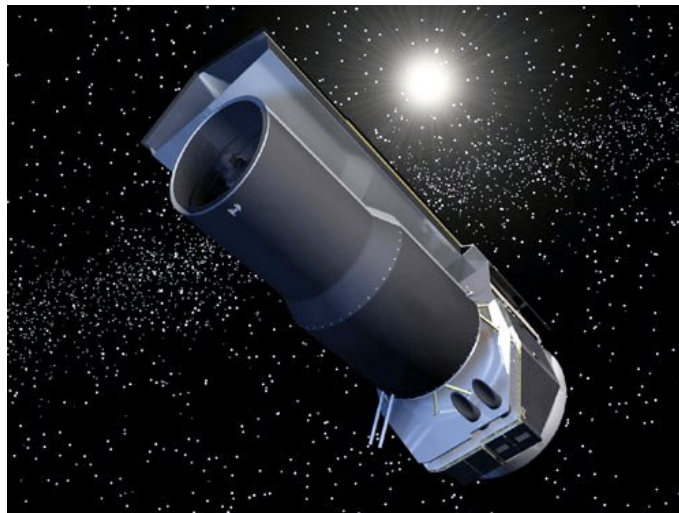


Figure 1.3: The Spitzer Space Telescope. credit:coolcosmos (2004)

The observations used in this thesis were obtained with the PACS, SPIRE and MIPS instruments.

## 1.3 The Life of Stars - a Brief Review

### 1.3.1 Formation and Evolution

Stars are born and form within clouds of interstellar gas and dust in dense molecular regions. These clouds have masses between  $\sim 10^4 M_\odot$  to  $\sim 10^6 M_\odot$  and sizes between 20 to 100pc. The temperatures can be extremely cold ( $\sim 15$  K), and the volume-averaged densities can be up to 100 molecules/cm<sup>3</sup> (Beuther et al. (2006)). At these temperatures, the atoms bind together and the gases become molecular.

The molecular clouds are highly turbulent and fragmented, consisting of clumps and cores. Typically, these clumps are thousands of solar masses, have typical sizes of 1 pc, volume densities of  $\sim 10^5$ – $10^9$  H atoms/cm<sup>3</sup> (Motte et al. (1998)), mean column densities of  $\sim 1$  g/cm<sup>2</sup>, visual extinction of hundreds of magnitudes and velocity dispersion of a factor of a few, several km/s (e.g. Krumholz (2006), McKee and Tan (2002)).

The cores have smaller radii and higher densities and volumes than the massive clumps around them,  $10^6$  cm<sup>3</sup>. The physical characteristics of the cores mark them as candidates to be the progenitors of massive stars and may in return determine the properties of the stars they form. (e.g. Garay (2005)).

The molecular clouds are subject to turbulence deep within them (e.g. Goldreich and Kwan (1974), Elmegreen and Falgarone (1996), Norman and Ferrara (1996)). This turbulence is a highly supersonic phenomena that converts kinetic energy into thermal energy on large scales Ballesteros-Paredes et al. (2007). Turbulence deep within molecular clouds could arise due to collision with other clouds (e.g. Heitsch et al. (2005), Inoue and Fukui (2013)), or due to shocks, for example from gas-flows when pushed into colder and denser regions in the interstellar medium, shocks from jet flows produced by stars while being formed (Seeds and Backman (2012)), shocks from nearby supernovae explosions (de Avillez and Breitschwerdt (2005)), or shocks from the passage of a molecular cloud through a galaxy having a spiral pattern Bonnell and Dobbs (2006). The perturbations unsettle the pressure equilibrium of the cloud, giving rise to clumps of sufficient mass ( $M \sim 0.25 M_\odot$ ) that the gas and dust begin to collapse under their own gravitational attraction (Larson (1981)). As the cloud collapses, the temperatures and densities at the center increase. When the inward gravitational pull balances the outward radiation pressure, an object called a protostar, is formed (Prialnik (2000)). The protostar is usually located inside a larger gas cloud and will be accreting matter from its surroundings. As a result, its mass will grow and the temperature and density of the core will increase. As the core heats up, a point is eventually reached when nuclear fusion starts taking place (Hydrogen fusion; where four hydrogen atoms create

one helium (He) atom associated with a release of energy). As the hydrogen depletes (converted to He), the number of particles then decreases, and the pressure drops, the core begins to collapse inward as the hydrostatic equilibrium shifts in favor of gravity. The fewer particles cannot maintain the needed pressure to support the star's outer layers. The contraction of the core slowly increases the pressure and temperature and with it a gradual increase of the core's power and the star's luminosity. The increased pressure on the layers just outside the core raises the temperature to a point where hydrogen fusion (hydrogen-shell burning) starts taking place in the layers. When the hydrogen is depleted in the innermost layers as well, the shells collapse upon the core raising the temperature and pressure of the core to a point where helium fusion is ignited (Kaufmann III (1988)). What happens next is determined by the initial mass of the star at formation.

## Low-Mass Stars

If a star's initial mass is less than  $8 M_{\odot}$  (low-mass stars, e.g. the Sun) then the helium core isn't hot enough for further fusion and so it contracts and heats up while hydrogen starts burning in a thin shell around the core. This causes the star to expand developing a convective envelope and the surface temperature to cool. The star becomes a luminous red giant. When the temperature of the helium core reaches 100 million degrees, helium fuses to make carbon (via the Triple Alfa reaction). Helium burning will further increase the central temperatures causing the core to expand violently. Shortly after the helium ignition, there is an explosion, the *helium flash*. The energy released by the helium flash is absorbed by the outer layers, so the star is not completely disrupted. To counteract the expansion of the core upon its increase of temperature, the outer layers contract and the luminosity drops. The high temperatures at the core also ignite secondary reactions to fuse oxygen from helium and carbon. The helium in the core runs out for the Triple-Alfa fusion, leaving a carbon-oxygen (CO) core and a helium burning shell outside the CO core, which contracts and heats. The shell around the core becomes unstable shedding its outer layers as an planetary nebula that is ionized by the increased number of photons flowing outward from the star's hot core. The shedding of the outer layers exposes the hot luminous core, which eventually cools to become a white dwarf (Karttunen et al. (2007)).

## High-Mass Stars

If a star's initial mass was around  $8 M_{\odot}$  (high-mass star), it will fuse hydrogen to helium using carbon, nitrogen and oxygen as catalysts (CNO cycle). When

the hydrogen is exhausted, high-mass stars convert helium atoms into carbon and oxygen explosively, *carbon* or *oxygen flash* just like helium flash. For even larger masses, as the core contracts and temperatures become higher, burning will continue. First carbon burning and successively oxygen and silicon burning will be ignited. As the nuclear fuel for each is depleted in the center, the burning will continue in a shell. The high-mass stars will have onion-like structure, with the core surrounded by consecutive shells carrying the products of the previous thermonuclear reactions. While the outermost layers may still be hydrogen-rich, the last element to undergo fusion into heavier elements in the core is iron (Fe). The nucleus of an iron atom is optimally stable; it has the highest binding energy per nucleon ratio than any other element in the periodic table. In order for iron to participate in any fusion process, more energy is needed to overcome the repulsive force between the protons of the iron nuclei than what is produced in the fusion process. Thus, this process consumes energy more than it produces which disrupts the support that prevented the star from imploding or exploding (Clayton (1968)). The temperature of the core rises and the core collapses as the pressure force can no longer balance out the gravity. The core compresses due to the collapse and becomes very dense. The collapsing continues until neutron degeneracy where protons and electrons combine to form neutrons. These stars will end their evolution as neutron stars or if the mass of the core is large enough, a black hole. The outer layers of the star will fall collapsing onto the dense central core and the material will heat up releasing an incredible amount of energy in the form of a massive bright explosion that blows off the outer layers followed by a powerful shock wave moving outward. This explosion is known as a Supernova (Seeds and Backman (2012)). Supernovae explosions, deposit tremendous amounts of mechanical energy into the ISM which in turn helps shape the energetics and structure of the ISM in galaxies. The supernova explosions eject large amounts of chemically-enriched gas into the interstellar medium. This ejected material is rich in heavy elements that were products of the thermonuclear processes in the interior of the massive stars. They are responsible for the enrichment of the interstellar medium releasing all the chemical elements heavier than iron in the universe, for example copper, gold, mercury, iodine, lead, etc . This provides raw material for the birth of new generations of stars playing a major role in star and planet formation. Moreover, elements heavier than iron can now be produced since their nucleosynthesis processes consume huge amounts of energy which the supernova can now provide (Hoyle and Fowler (1960)).

Depending on the mass of the star, high-mass stars can evolve into different types. Stars with masses between  $8M_{\odot}$  and  $20M_{\odot}$  evolve into the red supergiants (RSGs) which are cold stars (3500 - 4500 K) with enormous radii and might become blue supergiants (BSG) before returning to the RSG phase. If the star has a mass between  $20M_{\odot}$  and  $30M_{\odot}$ , it will end its evolution in the RSG

phase. More massive stars with  $>30 - 40M_{\odot}$  can become luminous blue variables (LBVs) which are extremely luminous and massive hot supergiants that lose a tremendous amount of their mass via strong stellar winds (Humphreys and Davidson (1994)). Stars with masses greater than  $40 M_{\odot}$ , can become a Wolf-Rayet (WR) stars which are extremely hot (30,000 – 200,000) evolved massive stars (Sander et al. (2012)).

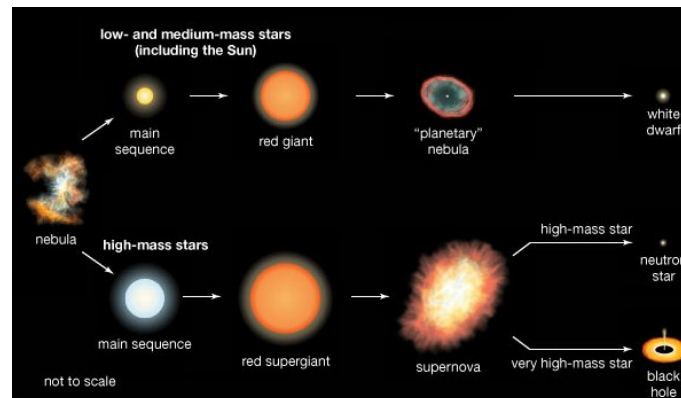


Figure 1.4: The stellar evolution of low-mass stars and high-mass stars

## The Rotation of Stars and its Effect on their Evolution

All clouds rotate due to the rotation of the galaxy in which they form. Any rotating object has an angular momentum, thus as the cloud collapses, it shrinks in radius and rotates faster and faster due to the conservation of angular momentum. Eventually, a flattened disk is formed that is slowly spiraling onto the central protostar. All stars spin due to the original angular momentum of the cloud in which it formed (e.g. Bally and Reipurth (2006), ichiro Inutsuka (2012)).

Massive stars rotate rapidly with equatorial rotation velocities 100–400 km/s (e.g Langer and Heger (1997), Mezzacappa and Fuller (2005)). The rotation can have several effects on the star, from its chemical composition to its lifetime.

As discussed extensively by Maeder and Meynet (2011), the rapid rotation of the massive star adds a centrifugal term to the equipotential surface of the star which varies with latitude (see Eq. 5 in Maeder and Meynet (2011)). This term expressing the force drawing the rotational body away from the center of rotation, affects the shape of the star in a way that the equatorial radius increases relative to the polar radius as the rotational velocity of the star increases (Georgy et al. (2010)).

Rotation also gives rise to anisotropies in the stellar wind which results in an asymmetric mass loss. The rotating polar regions have higher effective gravity, so the mass flux is enhanced at the poles. They also have higher effective temperatures, so the radiation pressure is stronger at the poles, these two characteristics causes the resulting nebulae to have a peanut-shape. However, for lower effective temperatures ( $T_{eff} = 24000\text{K}$ ) the opacity is higher between the pole and the equator, resulting in increased mass loss at the equator with the formation of a disc. (Georgy et al. (2010)).

Moreover, the rotation induces circular currents inside the star that redistributes heavy elements. Heavier elements formed in the core diffuse up to the surface (Maeder et al. (2006)).

Another effect is the magnetic fields which allow for the coupling between the interior of the star and its wind enhancing the loss of angular momentum and eventually slowing the speed of its rotation (Kawaler (1988), Heger et al. (2000)).

The fast rotating massive stars are thought to end their lives as supernovae. When a star is a part of a binary system, it evolves differently than when it is a single star system (Han et al. (2009)). How the pair evolves depends on the distance separating them. If wide, little effects are observed, however, if close, the effects have influence on their composition, lifetimes, luminosity, and surface temperatures.

## 1.4 Stellar Winds

As stars evolve, they shed mass via stellar winds. Stellar winds are characterized by continuous moving outflows of material with speeds of 10 km/s for a cool supergiant star up to 3,000 km/s for a hot luminous star (Lamers and Cassinelli (1999)). There are two basic parameters that are fundamental when observing stellar winds. The first parameter is the mass-loss rate, or the amount of mass-loss per unit of time. Stars evolve differently, they will thus have different mass-loss rates. The second parameter is the velocity the ejected material will have at large distances from the star, also known as the terminal velocity of the wind. This gives indication about the ejection mechanism since different ejections have different velocities (Lamers and Cassinelli (1999)).

Stellar winds differ for each type of star. Low-mass (relatively) cool stars eject tiny amounts of their mass per year (but still millions of tons of material each second) via their stellar winds, and only effectively nearing the end of their evolution while hot luminous massive stars have much stronger winds than those of low-mass stars, ejecting a few tens of solar masses in the form of high-speed

stellar winds (Lamers and Cassinelli (1999)). Stellar winds have different driving mechanisms. They are either pressure-driven due to the thermal pressure expansion of the extremely hot outermost layers of the star, wave-driven due to the dissipated energy from the surface of the star, or radiation-driven due to the radiation pressure of the photons escaping the star (Gail and Sedlmayr (2013)).

Stellar winds eject tremendous amounts worth of material from the star. This mass loss has numerous effects on stellar evolution (e.g. Renzini (1981), Chiosi and Maeder (1986), Blöcker (1995)). One of the effects is observed in the surface composition of the star. Nuclear fusion inside the stars changes the chemical composition and abundance of elements in the layers where fusion occurs. Where convection takes place, the products of nuclear burning will mix with the original elements in the convective regions. When the outer layers of the star are blown away, the products of the nuclear burning will appear at the surface showing over-abundances in heavy elements and changes in chemical composition. Another effect is the formation of white-dwarfs. The mass loss during the late-evolutionary phase of the star determines its fate. The final mass of a white-dwarf is below ( $<1.4 M_{\odot}$ ). This shows that low-mass stars ( $<8 M_{\odot}$ ) have lost most of their mass during their evolution which prevented them from evolving into supernovae (Lamers and Cassinelli (1999)).

The determination of stellar wind properties can be inferred from observation methods of spectral lines, for hot stars from UV and optical emission lines and for cool stars from molecular lines. The amount of gas and dust can be estimated via the IR continuum radiation. These methods can determine the stellar wind parameters. Stellar winds deposit enriched materials into the interstellar medium. If the winds are fast, there is a possibility they could collide with previously ejected winds, causing hot bubbles around hot stars, ring nebulae around WR stars, and compact HII regions (see section 2.2).

## 1.5 Dust Emission

Dust grains, formed by the aggregation of metals injected into the ISM by massive stars through stellar winds (Höfner (2009)), or less massive stars in their final evolution stages (Galliano et al. (2008)), or supernovae (Clayton et al. (1998)), absorb energetic photons which causes them to heat up. Processes like radiation emitted from nearby hot stars or collision with gas and other dust grains, heat up the dust grains, and much of this energy gained is reradiated as thermal emission at far-IR (FIR) and sub-mm wavelengths (Draine (2003)).

At long wavelengths (FIR and sub-mm wavelengths), the emission from the dust

grains radiate as a modified blackbody (also known as "grey body"), i.e it radiates with an emissivity factor (sometimes referred to as the dust "absorption cross-section") multiplied by the blackbody formula (Planck function) (Hildebrand (1983)).

$$F(\nu) = B_\lambda(T) \times Q(\lambda) \quad (1.1)$$

where:

$B_\lambda(T)$  is the blackbody intensity of temperature  $T$  at wavelength  $\lambda$ . A blackbody is a perfect absorber and emitter of radiation that depends only on the temperature of the body, and not its shape, material or constituents. The Planck function for a blackbody in units of  $Wm^{-3}$  is given by:

$$B_\lambda(T) = \frac{2hc^2}{\lambda^5} \frac{1}{e^{(hc/\lambda kT)} - 1} \quad (1.2)$$

$h = 6.63 \times 10^{-34} Js =$  Planck constant

$c \approx 3 \times 10^8 ms^{-1} =$  speed of light

$k = 1.38 \times 10^{-23} JK^{-1} =$  Boltzmann constant

And  $Q(\lambda)$  is the emissivity term given by:

$$Q(\lambda) = \left( \frac{\lambda_0}{\lambda} \right)^\beta \quad (1.3)$$

where:

$\lambda$  is the observed wavelength,  $\lambda_0$  is the reference wavelength,  $Q(\lambda)$  is dimensionless function which gives information about the mass/volume and emitting surface area of a typical dust grain and  $\beta$  is the power-law emissivity index dependent on the size and composition and equilibrium temperature (e.g. Draine and Lee (1984), Mennella et al. (1998), Jones and Jones (2002)) of the dust grains and is believed to lie between 1 for amorphous carbon grains (e.g. Koike et al. (1980)) and 2 for amorphous silicates and graphite grains (e.g. Rowan-Robinson (1986)). The spectral index  $\beta$  of a dust grain encode information about its chemical nature and its physical properties.

On the other hand, there could be a notable variation in the dust emissivity when considering the physical properties. Dust grains don't hold the same sizes and composition and thus absorption coefficients, this in turn affects the emissivity index. For this reason, modified blackbodies are regarded as simple models that cannot reproduce absolute values but only an estimation.

In the treatment of the infrared dust, we assume an optically thin regime where the effects of scattering and absorption can be ignored based on the small chances of a photon interacting with a dust grain. This approach is also assumed in hopes of measuring the amount of radiation emitted directly by the object as opposed to its emission being immediately absorbed by the surrounding grains. This assumption is advantageous to studying the emission throughout the entire object contrary to studying it just from the surface.

And so emission from the dust  $F(\nu) \propto B_\lambda(T_d) \times \left(\frac{\lambda_0}{\lambda}\right)^\beta$

Such model provides estimates of the dust temperature and the infrared emission.

## 1.6 The Spectral Energy Distribution of Dust

SED or a Spectral Energy Distribution resembles a blackbody function. It is a graph showing how the flux density ( $F_\nu$ ) (or energy) emitted by an object varies with wavelength ( $\lambda$ ). The units most frequently used for flux density are Janskys Haddock (1958). A Jansky (Jy) is:

$$1\text{Jy} = 10^{-26} \frac{\text{W}}{\text{m}^2\text{Hz}} (\text{SI}) = 10^{-23} \frac{\text{erg}}{\text{s cm}^2\text{Hz}} (\text{cgs}) \quad (1.4)$$

As mentioned in the previous section, thermal emission from dust is predominant at IR and sub-mm wavelengths. Consequently, properties of the IR and sub-mm SED can provide essential information about the state of the dust.

There are four main characteristics of a dust SED:

- [1] At the shortest wavelengths of the spectrum, the energy distribution is only that of a star. The dust only contributes at the longer wavelengths. If we consider a star surrounded by its stellar wind, the total flux emitted by a star plus its wind would not surpass the flux emitted by the star itself, since the dust absorbs the short stellar radiation and emits them in the infrared.
- [2] The dust SED has a characteristic peak (bump) in the IR and it is linked to the effective temperature of the dust. Hotter grains tend to peak at shorter wavelengths (few microns). Different regions of circumstellar dust emit at different wavelengths. The near-IR wavelengths trace emission from warm inner regions that are close to the surface of the star while the far-IR and sub-mm wavelengths trace cool outer regions. Thus, the peak of

the dust SED is indicative of the dust shell radius. If the radius of the dust shell has moved to further distances, the effective temperature of the dust will drop (since the temperature of the particles will decrease with distance from the heating source), and the peak will move to longer wavelengths (see fig.1.5).

- [3] The dust energy distribution at wavelengths further out the peak can be approximated by a power-law with a slope that depends on  $\beta$ .
- [4] The radiation of the dust at very long wavelengths decreases zero (not shown in fig. 1.5).

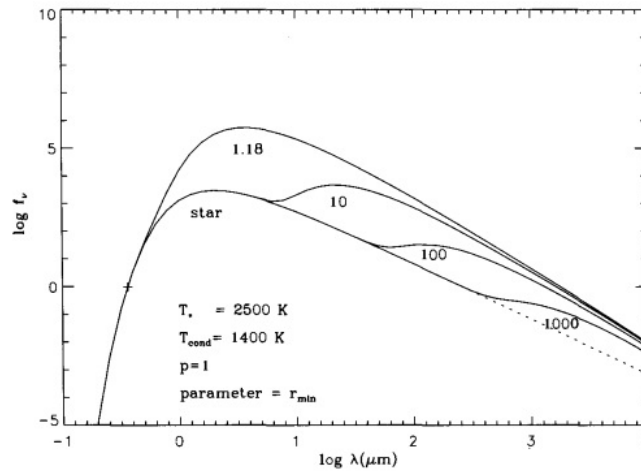


Figure 1.5: The theoretical energy distribution with  $\beta = 1$  and a single temperature  $T = 2500\text{K}$  for different values of dust shell radii ( $r_{min}$ ). credit:Lamers and Cassinelli (1999)

Based on this, studying the entire (IR to sub-mm) SED can give insight about the minimum and maximum radius of the dust shell, the dust mass, the dust temperature distribution, and the emissivity spectral index since these parameters play a vital role in in the emission of dust.

## 1.7 Estimating the Dust Mass

If we consider a cloud with  $N$  dust particles of spherical geometry and cross section  $\sigma = \pi a^2$ , having a uniform size, composition and a single temperature  $T_d$  and where the dust distribution is optically thin at long wavelengths and is heated internally, the emission spectrum of the cloud can be fitted by the product (sec. 1.6):

$$B_{\lambda}(T_d) Q(\lambda)$$

If  $D$  is the distance to the cloud from the observer, then the flux density from the cloud is:

$$F(\nu) = N \left( \frac{\sigma}{D^2} \right) Q(\lambda) B_{\lambda}(T_d) \quad (1.5)$$

From eq. 1.5,  $N$  can be expressed as:

$$N = \frac{F(\nu) D^2}{B_{\lambda}(T_d) \sigma Q(\lambda)} \quad (1.6)$$

The volume of the dust cloud is given by:

$$V = N \nu \quad (1.7)$$

where  $\nu$  is the volume of the individual grain.

Thus  $V$ :

$$V = \frac{F(\nu) D^2}{B_{\lambda}(T) \sigma Q(\lambda)} \nu \quad (1.8)$$

Given a grain density  $\rho$  and dust mass  $M_d = V\rho$  where  $V = \frac{3}{4}\pi a^3$ ,  $M_d$  can be written as:

$$M_d = \left( \frac{F(\nu) D^2}{B_{\lambda}(T)} \right) \left( \frac{4}{3} \frac{a}{Q(\lambda)} \right) \rho \quad (1.9)$$

which can also be expressed by:

$$M_d = \frac{F(\nu) D^2}{B_{\lambda}(T_d) \kappa_d} \quad (1.10)$$

$\kappa_d$  is the grain mass absorption coefficient:

$$\kappa_d = \frac{3}{4\rho} \frac{Q(\lambda)}{a} \quad (1.11)$$

(see also, Hildebrand (1983)).

Estimating  $M_d$  depends on  $\kappa_d$  which in turn depends on the geometry of the dust grains. For the sake of straightforward analytic solutions, dust grains are usually considered to be spherical. However, in reality, dust grains are more likely to be irregular in shape. Thus uncertainties in the geometrical aspect of dust grains, whether in shape or size, will give rise to uncertainties in the  $\left(\frac{Q(\lambda)}{a}\right)$  parameter, and thus uncertainties in the estimation of the dust mass.

From eq. 4.8,  $\kappa_d$  also depends on  $Q(\lambda)$  which has a wavelength dependence. Thus accurate measurements of  $Q(\lambda)$  will improve mass determinations.

Thus, the uncertainties in  $M_d$  estimations primarily arise from the uncertainties of the considered dust species, the assumed dust absorption coefficient, and the unknown grain size distribution.



# Chapter 2

## Theory

### 2.1 Cosmic Dust from Massive Stars

Dust is a fundamental contributor to the formation, evolution and appearance of the Universe. Dust plays an important role in the evolution of galaxies, in absorbing, scattering and emitting radiation, in heating the interstellar gas, in driving the mass loss of evolved stars from their surface, and in the formation of stars and planets.

Despite studies confirming the existence of dust in the universe (e.g. Willson (2000), Matsuura et al. (2011), Gall et al. (2010)), its origin and evolution remains ambiguous.

Two possibilities are regarded as the prime providers of high amounts of dust: i) Supernovae (SNe) (Draine (2009)) and ii) evolving low-mass stars, the Asymptotic Giant Branch (AGB) stars (Andersen (2007)). However, in the former, it is argued that reverse shock waves in supernovae remnants are likely to destroy the dust formed in the supernovae (Bianchi and Schneider (2007)). There is also lack of observational evidence that supports SNe being important contributors of dust; observations showed only about  $10^{-3}M_{\odot}$  of dust from SNe (Rho et al. (2008), Meikle et al. (2007)). On the other hand, for the case of AGB stars, the evolutionary timescales for low-mass stars cannot support the high production of dust (Massey et al. (2005)).

Dust production requires environments of high gas densities,  $\log n(\text{H}) > 10^8 \text{ cm}^{-3}$ , and relatively low temperatures  $< 2000 \text{ K}$  (Sedlmayr (1994)). The interstellar medium is not a suitable location for dust formation since the process would take an excessive time to be accomplished (Evans (1993)). The condensation timescales must be shorter than timescales of processes that favor the grain's growth.

Depending on the environment where dust grains condense, different dust species will result. The environments can either be oxygen-rich, or carbon-rich and depending on the most abundant elements in each environment, either silicates of carbon dust will form.

Examples of dust species for an environment:

- Oxygen-rich:
  - Silicates: olivine ( $[\text{Mg, Fe}]_2\text{SiO}_4$ ), forestite ( $\text{Mg}_2\text{SiO}_4$ ), pyroxene ( $[\text{Mg, Fe}]_2\text{SiO}_3$ ), enstatite ( $\text{MgSiO}_3$ ), magnetite ( $\text{Fe}_3\text{O}_4$ ).
  - Carbonates: corundum ( $\text{Al}_2\text{O}_3$ ), spinel ( $\text{MgAl}_2\text{O}_4$ ), titanium oxide ( $\text{CaAl}_{12}\text{O}_{19}$ ),  $[\text{Mg, Fe}]\text{O}$  or  $\text{SiO}$  grains.
- Carbon-rich:
  - Amorphous carbon, graphite, nano-diamond.
  - Silicon carbide ( $\text{SiC}$ ),  $\text{FeS}$  or  $\text{MgS}$  grains.

Recently (2010), lights have been shed on the role of massive stars regarding their contribution to the dust reservoir, particularly when observations have indicated that these stars lose intensely a high fraction of their mass via stellar wind and outbursts (e.g. Gvaramadze et al. (2010), Wachter et al. (2010)). This high dust contribution given their (relatively) short lifespans make them interesting to study. Thus, massive stars may contribute to the dust mass budget of the universe right before and after their explosions as SNe. This marks them as highly important to explore.

## 2.2 Circumstellar Material around Different Types of Evolved Massive Stars

There two main ways through which stars interact with the ISM. First, through their ionizing radiation, and second, through the mass, momentum and energy deposited via their winds.

As discussed in 1.3.1, low-mass stars lead to the formation of planetary nebulae that is ionized by the radiation from the star's core. For the case of high-mass stars, the mass-loss associated with their winds interact with the interstellar medium and leads to the formation of 'wind-bubbles'. More massive stars have the greatest effect on the ISM. Characterized by high mass-loss rates and very fast winds, massive stars exhibit a variety of circumstellar material around them.

However, the stellar winds are not all of same parameters, as a matter of fact, they depend on the status of the central star. Hydrodynamic instabilities within the star might change the dynamical properties of the wind. Density inhomogeneities and asymmetric winds may alter the morphology of the resulting circumstellar nebulae. These factors in turn change as the star evolves, therefore the interaction of the stellar winds with the interstellar medium will be unique depending on which life stage the star is at (Dwarkadas (2006)).

Moreover, not all massive stars are surrounded by detectable circumstellar nebulae. A dense shell of circumstellar material can form for two reasons: One, due to a sudden explosion that blows off a large amount of ejecta from the star. Two, if a fast stellar wind sweeps up the material of a previous blown slow stellar wind. By any means, the presence of nebula is dependent on significant mass-loss during short periods. This is the main reason why circumstellar nebulae are linked to evolved massive stars since these type of stars experience remarkable mass loss during their late transitional periods.

## Main-Sequence O Stars

The main-sequence (MS) stage of a star is the stage where it spends most of its life. During the MS phase, the star is in stable equilibrium and the only source of stellar energy is that which is released by hydrogen burning in the core. O-type MS stars are very hot and extremely luminous stars radiating mostly at short wavelengths, so they appear bluish. These stars are very rare.

MS O stars have fast stellar winds of very high velocities ( $v > 1,000\text{--}2000$  km/s). When these stellar winds expand, they sweep off material from the surrounding ISM and form interstellar bubbles, called wind-blown bubbles (WBB) (Weaver et al. (1977)). A WBB consists of a cavity surrounded by a thin expanding shell of swept up ionized gas (see Fig. 2.2).

At a certain distance from the star, the ejected material achieves supersonic speeds and creates a shock upon interacting with the surrounding medium. This interaction between the wind and the ISM leads to significant heating of both the shocked wind and the ejected material. The wind sweeps up the gas and the dust material from the interstellar material and gathers them into a hot layer. This hot layer tends to expand in two directions: i) outward towards the ISM and ii) inwards back into the wind. This ultimately produces *two shocks*, on the inside and the outside and eventually the hot layer forms an interstellar bubble Weaver et al. (1977).

The dynamical shaping of the interstellar bubble comes as follows: As the stellar wind moves away from the star with constant velocity, its density decreases. This is called the free-streaming wind which itself forms the next two consec-

utive zones. The following region contains the compressed wind gas that has been heated when the wind had passed through the wind termination shock. The termination shock is the boundary at which the stellar wind particles slow down to the point where they are traveling slower than the speed of sound. The next region consists of the shocked interstellar material that is swept up into a an expanding shell expanding driven away by the thermal pressure of the hot bubble. After that comes the (not yet) undisturbed interstellar medium into which the expanding shell moves (Weaver et al. (1977)). Hot massive stars also emit high-energy photons that are capable of ionizing the HII region. The WBB associated with main-sequence stars now has an inner part consisting of the hot shocked material and an outer part consisting of the cold photo-ionized interstellar medium separated by contact discontinuity (see Fig. 2.1).

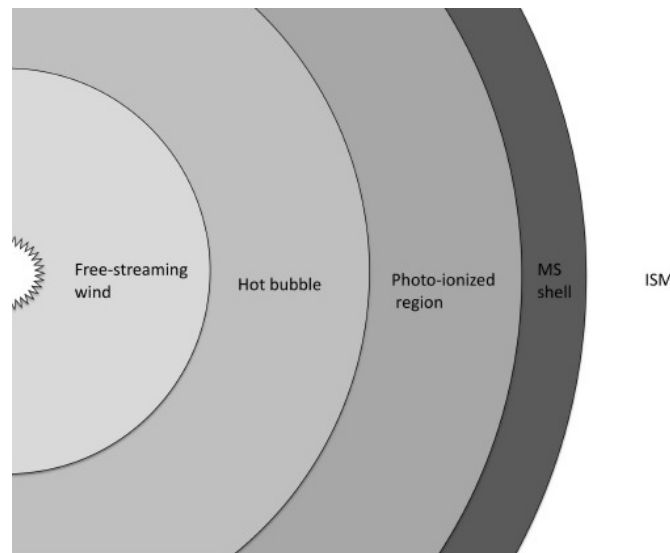


Figure 2.1: The dynamical shaping of the main-sequence interstellar bubble.

However, the morphology of the WBB is hardly observed around MS O stars. The circumstellar material indicating their existence are rarely detected. An observation of the HII star-forming region, N11B, in the Large Magellanic Cloud (LMC), spectroscopically revealed expanding shells around O stars, having velocities (10–15 km/s) slightly higher than the isothermal sound velocity ( $\sim 10$  km/s) (Alfaro et al. (2004)) of the surrounding HII ionized gas ( $10^4$  K). Thus, these expanding shells cannot produce strong shock waves to allow enough compression of the material which in turn should enhance its degree of emission. The density contrast needed to show a ring nebula morphology is thus not achieved.

However, in later evolutionary stages of the star when it can no longer ionize the shell around it, the interstellar bubbles might become observable. At some point, the velocity of the expanding shell ( $\sim 10$  km/s) will be higher than that



Figure 2.2: The Bubble Nebula (NGC 7635) created by the O-class star BD+60°2522. credit:apod (2013)

of the isothermal sound velocity ( $\sim 1$  km/s) of the neutral HI medium (100 K), which permits a strong compression wave producing noticeable shell morphology ( $10^3$  pc) (Nazé et al. (2001)).

## Red Supergiants

Stars with masses between  $8 M_{\odot}$  and  $20 M_{\odot}$  evolve into red supergiants (RSGs) which are cold stars with effective temperatures 3500 - 4500 and enormous radii ranging from 500 to  $1500 R_{\odot}$  ( $1 R_{\odot} = 6.955 \times 10^5$  km) and yield high mass-loss rates ranging from  $10^{-6}$  to  $10^{-4} M_{\odot} \text{yr}^{-1}$  (Maunon and Josselin (2010)).

Unlike the case with MS O stars, when a star later becomes a RSG, it loses its mass via slow ( $10$ – $15$  km/s) dense winds and gathers its material into a circumstellar nebula (García-Segura and Mac Low (1993)). Since the RSG winds are much slower than that of MS stars, they will not form wind-blown bubbles. However, the ejected circumstellar material is sometimes observed in extreme or nearby cases that are marked by very strong mass-loss episodes. An example of this is the red supergiant VY Canis Majoris. The result of these enhanced ejections are seen as a circumstellar reflection nebula detected at optical and IR wavelengths enhanced by the effects of dust scattering and the thermal continuum emission from the dust grains (Smith et al. (2001)) (see Fig. 2.3). Another example of a red supergiant is Betelgeuse. Despite it being at close distances ( $150$ – $200$  pc), its circumstellar material is hard to detect because its mass loss rate is not significant. (Harper et al. (2008))

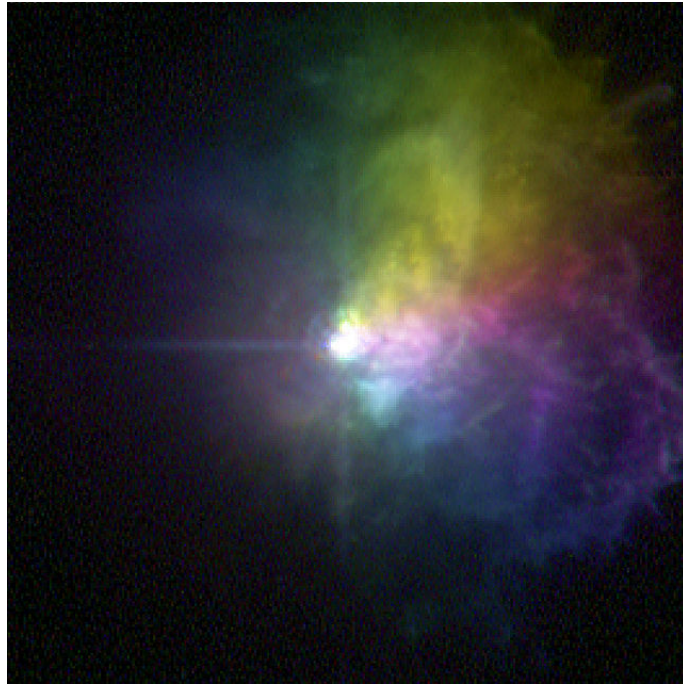


Figure 2.3: VY Canis Majoris, an extreme red supergiant blows off huge amounts of ejecta during one of its outbursts. credit: NASA (2007)

## Blue Supergiants

RSGs might become blue supergiants (BSGs) before returning to the RSG phase. BSGs are hotter (30,000 to 50,000K) than RSGs but smaller in size (up to  $25 R_{\odot}$ ). The circumstellar nebulae around the massive BSGs are not completely understood as only few attempts have been made to understand the structures (e.g. Blondin and Lundqvist (1993), Martin and Arnett (1993)). A BSG has fast winds ( $\sim 1000$  km/s) and is characterized by an equatorial ring (see fig.2.4) in the circumstellar nebulae formed either from enhanced outflows from the equatorial regions caused by the rapid rotation of the BSGs (Cassinelli (1998)) or as a result of the interaction between the previous RSG wind and the BSG wind or due to binary-system interactions where the mass transfer or the focusing of the wind in the equatorial plane are responsible for keeping the material in orbit around the system (de Wit et al. (2014)).

## Luminous Blue Variables

Stars with masses of  $30 - 40M_{\odot}$  can become luminous blue variables (LBVs). LBVs are hot (12,000 to 30,000K) massive and unstable stars that suffer irregular eruptions. They are characterized by high luminosities and high mass-loss

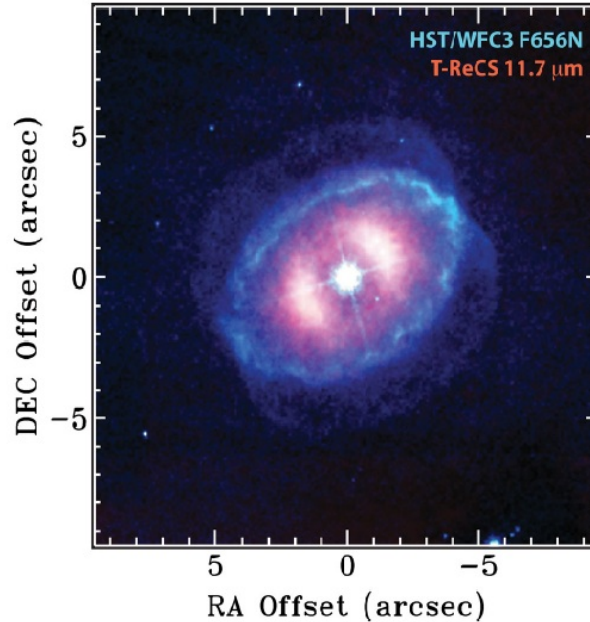


Figure 2.4: A colour-composite of the ring nebula around the BSG: SBW1. credit: Smith et al. (2012)

rates ( $10^{-5}$  to  $10^{-4}$  e.g. (Humphreys and Davidson (1994)) and significant spectral and photometric variability. They exhibit occasional energetic mass-loss outbursts, with the Great Eruption of  $\eta$  Carinae in the 1840s being an example. The material ejected eventually results in the formation of nebulae with a bare (WR star) core. These circumstellar nebulae or shells are thought to be expanding rapidly at a velocity  $25 - 140$  km/s with typical diameters of  $0.5 - 2$  pc (e.g. Lamers et al. (2001)). As for the case LBVs, the surrounding circumstellar nebulae are either due to long periods of high mass loss via slow and dense dust outflow or due to massive eruptions in brief intervals of time. LBV nebulae resemble the most known circumstellar nebulae around evolved massive stars.  $\eta$  Carinae (Morse et al. (1998)) and the Pistol star (Figer (1999)) are two examples of well-studied LBVs with nebulae (see Fig. 2.5). It is believed that LBVs are the greatest injectors of circumstellar material (Maeder (1998)). The nebulae associated with those type of massive stars can be enormous with masses  $10 - 20 M_{\odot}$  indicating an extremely intense and eruptive mass loss history (Smith and Owocki (2006)). However, some are smaller, of the order  $0.5 M_{\odot}$  like that of  $\eta$  Carinae after undergoing its second eruption in 1890 (Smith et al. (1998)) whereas it ejected at least  $10 M_{\odot}$  in its first eruption in 1840 (Smith et al. (2003)). While the  $\eta$  Carinae nebula is of bipolar shape (Weis et al. (1997)), another LBV, HD 168625, shows a triple-ring structures nebula (Smith (2007)), while P Cygni is spherical (Smith and Hartigan (2006)).

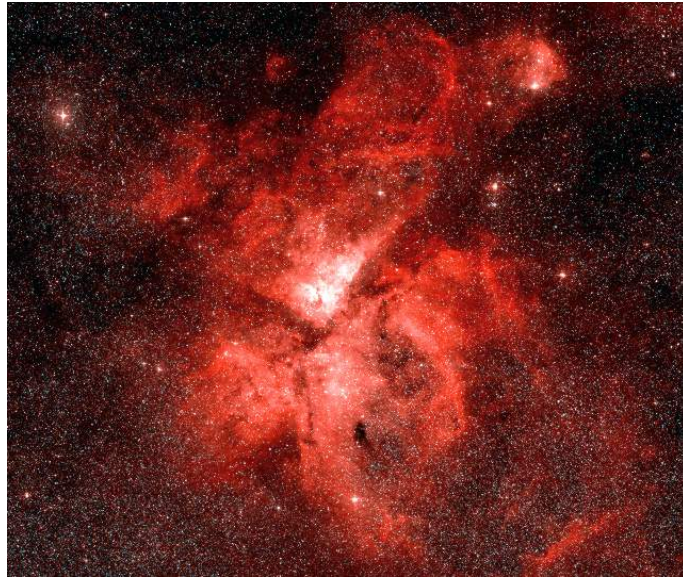


Figure 2.5: The huge Eta Carinae nebula. credit:AAO (2010)

## Wolf-Rayet Stars

More massive stars with mass greater than  $40M_{\odot}$  can become Wolf-Rayet (WR) stars (Marston et al. (1994)). WR stars possess extremely strong stellar winds (e.g.  $\approx 6,000\text{km/s}$  for the Galactic WO star WR93b Drew et al. (2004)) and high mass loss rates  $\approx (10^{-5}M_{\odot})$  (e.g. Nugis and Lamers (2002)). WR stars exhibit different types of circumstellar nebulae. One type is the large circumstellar bubble. The fast WR wind sweeps off the previously bulk ejections of either the RSG or LBV phase and pile them up into a shell or a circumstellar bubble (Stock and Barlow (2010)). A well-known example is NGC 6888 (see Fig. 2.6). The other type is the ring nebulae or, the "pinwheel" nebula forms upon the compression and cooling of the dust spewed out off from a binary star system with the WR wind when they collide together, and forming shockwaves as a result (Williams et al. (2001), (Garcia-Segura and Mac Low (1995)).



Figure 2.6: A Wolf-Rayet nebula: The Crescent Nebula (NGC 6888). credit: Hallas (2008)

## 2.3 Detection Methods

Detecting circumstellar dust shells is not easy, since most of the times they are located around very luminous stars. Other factors such as how far the circumstellar material is located from the luminous central source and how dense the material expelled from the star is, play an important role in whether the circumstellar shell is detected or not. For detection, the densities of the ejected material should be much greater in magnitude than the densities of the normal stellar winds expelling the material (Smith (2010)).

Visual wavelengths can be useful for detection in the cases where the nebula is sufficiently dense with the central star partially hidden by the circumstellar dust.

The near-IR wavelengths can observe massive stars that are obscured at the visual wavelengths.

The mid-IR and far-IR can easily observe the circumstellar dust shells because these wavelengths can penetrate the obscuring interstellar dust and detect the thermal-IR radiation emitted from the dust grains.

Longer mid-IR and far-IR are also useful since they can detect the cooler dust in the shells. Missions such as *Herschel* and *Spitzer* have allowed for these interesting detections by determine the dust emission as a function of wavelength thus providing means to study the physical properties of the dust.

X-ray wavelengths are ineffectual in detecting the nebulae since for a nebulae to produce bright x-rays, it needs to possess strong shock waves and this is not common in massive stars.

Radio wavelengths are useful in studying rather than detecting the circumstellar nebulae since they can trace photoionized gas around hot massive stars and probe molecular shells around massive stars. This gives information about the structure of the shells and their expansion.

# Chapter 3

## Data Analysis

In this thesis, the target sample treated for inspection was drawn from previous studies presented in Gvaramadze et al. (2010).

Gvaramadze and his colleagues searched for circumstellar nebulae using the 24  $\mu\text{m}$  data obtained with *Spitzer's* MIPS. They have detected 115 circumstellar nebulae with central sources in the archival MIPS 24  $\mu\text{m}$ . The discovered circumstellar nebulae (see Fig.1 in Gvaramadze et al. (2010)) held morphological resemblance to nebulae associated with LBVs and late WN-type WR (WNL) stars in the Milky Way (MW) and the Large Magellanic Cloud (LMC). The interpretation of this was that the nature of the central stars must be evolved massive stars. To support this interpretation, they have searched for previously detected IR circumstellar nebulae around known LBVs and WN stars in the MW and the LMC using the MIPS 24  $\mu\text{m}$  data and presented the known nebulae in a list of figures (see Fig.2 in Gvaramadze et al. (2010)). Comparison between Fig.1 and Fig.2 in paper showed striking similarities. To confirm the nature of the central stars, they further carried out spectroscopic analysis of 24 of the central sources of the newly discovered nebulae most of which were verified to be candidate LBVs, blue supergiants, or WNL stars.

For the purpose of this thesis, I have obtained the 24  $\mu\text{m}$  data of the target sample performed by *Spitzer's* MIPS, the 70 and the 160  $\mu\text{m}$  by *Herschel's* PACs, and the 250  $\mu\text{m}$  by *Herschel's* SPIRE. The two subsections to follow contain more details of the sample selected and how the data was obtained.

Although *Spitzer's* observational abilities cover common wavelengths (3-180  $\mu\text{m}$ ) as *Herschel* (60-670  $\mu\text{m}$ ), *Herschel's* larger size is advantageous with respect to the much higher resolution at which it takes the images even at same wavelengths thus revealing more structural details. Fig.3.1 shows a comparison of the imaged M51 at 160  $\mu\text{m}$  by both *Spitzer's* MIPS and *Herschel's* PACS.

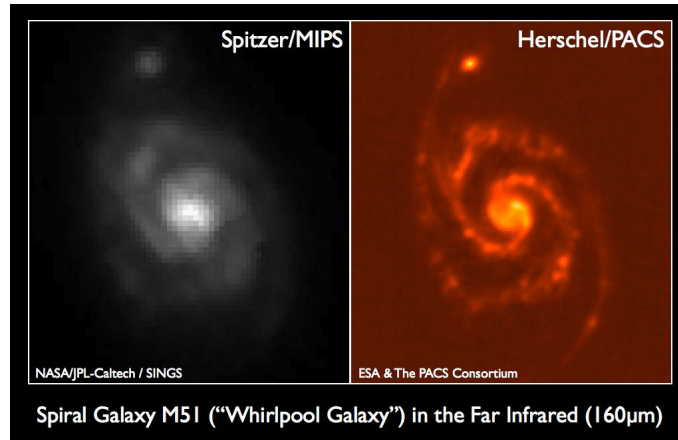


Figure 3.1: MN51 as seen by Herschel and Spitzer at the same band. credit: Siegel (2010)

## 3.1 Computational Tools

For the work of the data analysis, three software applications were used, SAOImage DS9, HIPE, and APT. This section briefly explains the function of each. Further details on how each was used in this thesis are mentioned in the following sections.

### 3.1.1 SAOImage DS9

The SAOImage DS9 is a display application designed specifically for astronomical imaging and data visualization. The software is distributed by Smithsonian Astrophysical Observatory of Cambridge, MA 02138 USA. DS9 is an image viewer software for the 'FITS' data format that is prevalent in the astronomical community. It has many features that allows for a wide range of scientific analysis. These features include inspecting images, manipulating regions and producing color maps. For more information, refer to the thorough DS9 user manual (Joye et al. (2013)).

In this thesis, DS9's basic features are used to visually investigate the data. The FITS files are obtained and opened with DS9. DS9 shows the full range of the image, from the brightest to the dimmest, set on a linear scale by default. This reveals very little features in the sky. The display range was thus constricted through the *Scale Parameters* option to bring out the lower-level data values. The latter was also done by using other non-linear scale types, such as the logarithmic scale which shows the dynamic range of the image more. To further enhance the display of the objects, the *Bias* and the *Contrast* are adjusted accordingly. Those two factors control the appearance of the color according to

pixel values.

To create RGB images, the three-color capabilities of ds9 are used. An RGB image is a three-color composite image in which Red, Green, and Blue are added together in various degrees to obtain a broad array of colors, hence the name. To make an RGB image for an object, three images of the same object taken with different wavelengths are needed. The data are loaded into a *new RGB* frame, and the frame contains all three files stacked together. However, each filter gives different information about the object. Therefore, to distinguish one from the other when put together, a different color is assigned to each wavelength of the different filters. Usually, longer wavelengths are 'red' colors, shorter wavelengths are 'blue', and the in-between wavelengths are 'green'. One can optionally choose to 'smooth' the data in order to bring out finer features by removing statistical noise. This is done by selecting the *Smooth Parameters* in the *Analysis* menu.

Another analysis tool that DS9 provides is overlaying astronomical data. DS9 allows for creating and displaying contours as an overlay on an image. Contours are curves drawn along pixels that have constant values. DS9 gives the user the option to specify the number of contour levels, how smooth the contours are, the flux at the lowest contour and the flux at the highest contour, also known as the contour scale. The generated contours can be copied and overlaid on top of another frame for comparison of data. By default, DS9 adjusts the size of the frames (images) and the center of the fields to be equal to each other when the two are overlaid.

### 3.1.2 HIPE

HIPE<sup>1</sup>, or the **Herschel Interactive Processing Environment**, is an application that allows users to work with *Herschel* data, including finding the data products, interactive analysis, plotting of data, and data manipulation. For this work, I have used HIPE to access data found in the online Herschel Science Archive (HSA). HSA is not a part of HIPE but it communicates with it. To obtain the data, I have entered the observation ID of the specific object in the corresponding field and retrieved the result into HIPE. HIPE allows for the inspection of the observation contents and data analysis such as fitting spectral features, or comparing with data from other observatories by importing non-Herschel FITS files or basic photometry, and reprocessing the data such as data reduction.

---

<sup>1</sup><http://www.cosmos.esa.int/web/herschel/hipe-download>

### 3.1.3 Aperture Photometry Tool

Aperture Photometry Tool (APT) is a software (Laher et al. (2012)) designed for the photometric exploration of astronomical scientific images. It allows aperture photometry calculations for point as well as extended sources. Aperture photometry calculations consist of measuring the brightness of an astronomical object contained within an aperture in the focal plane. The photometric calculations are done by measuring the source flux through summing the measured counts of the region within the aperture followed by subtracting the sky-background contribution which does not arise from the source itself. This yields then the target flux. Usually, the aperture chosen for the target is circular, while that of the sky-background is an annular ring.

Different models are available to carry out the sky background calculations (sky-background models). One of the models that is set by default in APT is the "No sky-background subtraction" (Model A) where the source photometric calculations are done without taking into consideration the sky contribution. However, the user can optionally choose one of three other models that accounts for the sky contribution when performing photometry. The models are the "Sky-median subtraction" (Model B), the "Sky-Average subtraction" (Model D) and the "Custom-Sky subtraction" (Model C) where custom pixel values can be specified to be rejected from the sky-background calculations. APT rejects all pixel values that are greater than 3 standard deviations from the median. This is hard-coded in APT and cannot be changed by the user. The *pick/zap* tool is another method in which pixels can be eliminated from the background calculations of interest. The median multiplied by the number of pixels in the aperture form a product which is then optionally subtracted from the data of the source. This then yields the background-subtracted source intensity.

For the source calculations, different models are also available (source models). The user can optionally choose between three models. One that does not interpolate for any pixels (Model 0), one that interpolates for all aperture pixels (Model 1), and one that interpolates for specified pixels only (Model 2).

APT provides the user with several graphs that are useful in determining the photometric parameters while performing the calculations. The "Curve of Growth" aids the user in determining the best sizes of the aperture and the sky-annulus. The "Aperture Slice" plot gives information about how well the aperture is centered. The "Source Scatter", "Sky Scatter", "Sky Histogram" are helpful in setting adequate pixel-rejection thresholds. (Include pictures).

APT also gives the user the opportunity to interpolate data using the radial profile function. The user can parametrize the profile to compute the photometry of the target of interest.

One important factor in performing the aperture photometry calculations in APT

is taking into account the data units of the image. Rejecting pixels specifically should be fed in APT with the same data units found in the header of the FITS file and then converting the whole image units to the desired source-intensity units.

## 3.2 *Spitzer Maps*

I have made use of The Spitzer Heritage Archive (SHA) interface<sup>2</sup> of the *Spitzer* telescope to obtain the 24  $\mu\text{m}$  data performed with the MIPS instrument. The interface provides public access to data done by MIPS GAL. MIPS GAL is the **24 and 70 Micron Survey of the Inner Galactic Disk** done using the MIPS instrument (Carey et al. (2009)). For each observation done, there are three types of files ready for download from the archive: RAW, BCD (Basic Calibrated Data) and post-BCD where each describes a different stage of reduction. The BCD data have the instrumental signatures removed and were calibrated into physical units where each pixel contains information about the detection.

In this thesis, I was mainly interested in the post-BCD data that were further reduced. The reduction processing accounted for corrections of the BCD images of several artifacts such as: cosmic ray hits, detecting outlier pixels, refining the pointing of the telescope, and producing mosaicked images.

Given the equatorial coordinates of the likely central sources associated with the nebulae found in Gvaramadze et al. (2010) (See Table 1 and Fig. 2 in paper), I have downloaded the 24  $\mu\text{m}$  post-BCD data which contained the mosaic images needed for analysis. The mosaic images are in FITS<sup>3</sup> format.

The temperature of the dust detected at 24  $\mu\text{m}$  is estimated to be 120.7 K according to Wien's displacement law (3.1). The latter describes the relationship between the temperature of a body and at what wavelength its emission peaks. This is given by:

$$\lambda_{peak} \times T = b \quad (3.1)$$

where  $\lambda_{peak}$  is the peak emission of a blackbody,  $T$  is the temperature of the body, and  $b = 2.897769 \times 10^{-3} m.K$  is Wien's displacement constant.

The temperature  $T$  varies inversely with the wavelength  $\lambda_{peak}$ . This means that as the temperature of the object cools, the emission from the object shows up more prominently at farther infrared wavelengths.

<sup>2</sup><http://archive.spitzer.caltech.edu/>

<sup>3</sup>FITS is a file format commonly adopted within the astronomical community for the transport, analysis, and archival storage of scientific data

The  $24\mu\text{m}$  data traces emission from relatively warmer dust.

### 3.3 *Herschel Maps*

I have used HIPE as the main tool to obtain the *Herschel* maps (see sec. 3.1.2). Via HIPE, I made use of The Herschel Science Archive (HSA)<sup>4</sup> of the *Herschel* telescope to obtain the 70 and  $160\mu\text{m}$  data performed with the PACS instrument, as well as the  $250\mu\text{m}$  data performed with the SPIRE instrument.

*Herschel's* archive can be accessed through Herschel's User Interface (HUI) which provides public access to data done by *Herschel*. For each observation done, there are five types of files ready for download from the archive: level-0, level-0.5, level-1, level-2, and level-3 where each describes a different stage of reduction.

Level-0 is the raw data. Level-0.5 is data that is converted to physical units where each pixel contains information about the detection. Level-1 have the satellite and instrumental effects removed. Level-2 are further processed ready for scientific analysis (e.g: maps). Level-3 are data combined with other theoretical models, laboratory models, observations and catalogues.

In this thesis, I was mainly interested in the level-2 data.

Given the equatorial coordinates of the likely central sources associated with the nebulae found in Gvaramadze et al. (2010), I have used SIMBAD's<sup>5</sup> coordinate query to obtain the 2MASS name for each object. 2MASS or the **Two Micron All-Sky Survey** was a survey of the whole sky in three infrared wavebands:  $1.25, 1.65$  and  $2.17\mu\text{m}$ . A catalog was made for the numerical description of each detected source that is put in a public domain (SIMBAD).

To download the Level-2 data, I have used the tool "Send to External Application" → "HIPE" provided by HUI to inspect the data and convert it to their FITS format.

According to Wien's Law (see 3.1), the temperature of the dust detected at 70, 160 and  $250\mu\text{m}$  is estimated to be 41, 18, and 12 K respectively.

The 70, 160 and  $250\mu\text{m}$  data trace emission from relatively colder dust.

---

<sup>4</sup><http://www.cosmos.esa.int/web/herschel/science-archive>

<sup>5</sup>SIMBAD is an astronomical database of objects beyond the Solar System and maintained by the Centre de donnees astronomiques de Strasbourg, France.

## 3.4 Selection of Sample

The downloaded images of the objects at their respective bands, were then visually inspected using the SAOImage DS9 software. This revealed a wide variety of compact nebulae having different morphology. Some appeared to be circular, some bilateral, and some bipolar.

While the majority of the objects in the 160  $\mu\text{m}$  and 250  $\mu\text{m}$  bands were not visible, the criterion for the selection of the sample was based on whether an object was detected in at least two of the four bands or not, *Spitzer's* 24  $\mu\text{m}$ , and *Herschel's* 70  $\mu\text{m}$ . This ensured the study of the sample in the mid- to far-infrared range.

After a thorough investigation on all the images, the sample studied in the course of this thesis therefore consists of 25 out of 133 objects. The 133 objects are those presented in Table 1 and Figure 2 in Gvaramadze et al. (2010).

## 3.5 Contours and RGB Images

To further investigate the dust emission, I have used SAOImage DS9 to apply intensity contours to trace the presence of warm dust and cold dust allowing for the comparison between the two.

Appendix A shows the images with the contours of both; *Spitzer's* MIPS 24  $\mu\text{m}$  tracing the warm dust and *Herschel's* PACS 70  $\mu\text{m}$  tracing the colder dust. The contours are overlaid.

Three-color RGB images for the sample were produced. The aim of this was to highlight differences in the dust emission. The blue color was assigned to the 24  $\mu\text{m}$  data, the green to the 70  $\mu\text{m}$  data, and the red to the 160  $\mu\text{m}$  data.

Following a visual inspection (by eye-detection) of the 25 RGB images, I chose 5 objects that exhibit the most symmetric shells (circular or very slightly elliptical). The 5 objects are: MN27, MN87, MN111, GAL024.73 + 00.69, and WR31a (see Appendix B for more information about each). There is a strong selection bias based on the (mentioned) morphology of the dust shells. Such symmetry is interesting because it suggests a previous spherically symmetric outflow, and that the dust shells are expanding symmetrically into the evacuated medium.

## 3.6 Source Detection and Photometry

I performed photometric analysis of the five objects using the Aperture Photometry Tool (APT) software. The aim of this analysis is to obtain the emission flux density of the 5 sources. Numerous parameters can be obtained from performing photometry. Based on the aim of this thesis, I will use the measured flux density for each source and their uncertainties obtained by the photometry for fitting SEDs which will eventually allow for the characterization of parameters such as the temperature and mass of the circumstellar dust shell surrounding the source.

### 3.6.1 Image Units Conversion

After obtaining the astronomical images of the sources, and before carrying on with the photometry, one has to make sure that the units of all the images obtained are the same. This should allow for the direct quantitative comparison of an object in images of different bands.

Different telescope arrays have different pixel sizes and thus the images created are of different pixel scales. Information about the pixel scale can be found in the FITS header of each image. The FITS header usually contains specifications such as size, origin, coordinates, comments and history of the image data.

Knowing this, I have retrieved information about the data from the FITS header of each image. The units of the PACS (70 and 160  $\mu\text{m}$ ) images are in Janskys per pixel ( $\text{Jy}/\text{px}$ ) while the units of the MIPS (24  $\mu\text{m}$ ) and SPIRE (250  $\mu\text{m}$ ) images are in MegaJanskys per steradians ( $\text{MJy}/\text{sr}$ ) where:

$1\text{MJy} = 10^6 \text{Jy}$ , and a sr is the SI unit of solid angle.

The information about the pixel scale are found under the keywords **CDELTA1** and **CDELTA2** in the FITS header corresponding to the rows and columns of the image in degrees per pixel ( $\text{deg}/\text{px}$ ). To convert the units of the image, I have proceeded in the following way:

For the MIPS images, **CDELTA1** =  $-0.000681$  [ $\text{deg}/\text{px}$ ] and **CDELTA2** =  $0.000681$  [ $\text{deg}/\text{px}$ ]. The negative sign of **CDELTA2** is a FITS convention. It will be ignored. These values inform us about the size of a pixel in the image.

To know the size of the pixels in square degrees per pixel<sup>6</sup>:

$$0.000681 \frac{\text{deg}}{\text{px}} \times 0.000681 \frac{\text{deg}}{\text{px}} = 4.63761 \times 10^{-7} \frac{\text{deg}^2}{\text{px}} \quad (3.2)$$

<sup>6</sup>[coolwiki.ipac.caltech.edu/index.php/Units](http://coolwiki.ipac.caltech.edu/index.php/Units)

The relation between square degrees and sr can be deduced from the following:

There are 60 arcminutes per one degree and 60 arcseconds per one arcminute, and so there are 3600 arcseconds per one degree:

$$\frac{60 \text{ arcminutes}}{1 \text{ deg}} \times \frac{60 \text{ arcseconds}}{1 \text{ arcminutes}} = \frac{3600 \text{ arcseconds}}{1 \text{ deg}} \quad (3.3)$$

Squaring yields:

$$(1 \text{ deg})^2 = (3600)^2 = 1.296 \times 10^7 \text{ arcsec}^2 \quad (3.4)$$

We know that:

$$1 \text{ steradians} = 4.25 \times 10^{10} \text{ arcsec}^2, \text{ so } 1 \text{ arcsec} = 2.3529412 \times 10^{-11}$$

To know how many sr are in  $\text{deg}^2$ :

$$1.296 \times 10^7 \frac{\text{arcsec}^2}{\text{deg}^2} \times 2.3529412 \times 10^{-11} \frac{\text{sr}}{\text{arcsec}} = 0.0003046118 \frac{\text{sr}}{\text{deg}^2} \quad (3.5)$$

To find out what the size of pixels are in sr:

$$4.63761 \times 10^{-7} \frac{\text{deg}^2}{\text{px}} \times 0.0003046118 \frac{\text{sr}}{\text{deg}^2} = 1.4124849 \times 10^{-10} \frac{\text{sr}}{\text{px}} \quad (3.6)$$

Finally, I convert the units of the image:

$$\frac{\text{MJy}}{\text{sr}} \times 1.4124849 \times 10^{-10} \frac{\text{sr}}{\text{px}} = 1.4124849 \times 10^{-10} \frac{\text{MJy}}{\text{px}} \quad (3.7)$$

To convert to Jy/px:

$$\frac{\text{MJy}}{\text{px}} \times 10^6 = \frac{\text{Jy}}{\text{px}} \quad (3.8)$$

And so Eq.3.7 becomes:

$$1.4124849 \times 10^{-10} \frac{\text{MJy}}{\text{px}} \times 10^6 = 1.4124849 \times 10^{-4} \frac{\text{Jy}}{\text{px}} \quad (3.9)$$

The result of this derivation yields a number that should transform the MIPS image data units from MJy/sr to Jy/px. This number is:  $1.4124849 \times 10^{-4}$  Jy/px.

The same procedure is followed for the SPIRE images which are in MJy/sr as well. For  $\text{CDELTA1} = -0.001666666666667$  and  $\text{CDELTA2} = 0.001666666666667$ , the conversion factor from MJy/sr to Jy/px is:  $8.4614151 \times 10^{-4}$ .

The PACS image data units are already in Jy/px and need no unit conversion.

### 3.6.2 MIPS-24 $\mu\text{m}$ and PACS-70 $\mu\text{m}$ Aperture Photometry

For each source, the aperture chosen was circular with an angular diameter to encompass most of the emission from the central source and no or little extra emission (and noise) from other background stars. The size (diameter) of the aperture was adjusted according to the size of each individual target in their respective image. To choose an optimal aperture radius, I made use of the Curve of Growth plot. This plot describes the variation of the total flux measured of a source as a function of the aperture radius. Thus, it gives an indication about the size of the aperture to be set. And so I chose it to be at a point which included nearly all the flux from the source and where the Curve of Growth leveled off almost evenly, see fig. 3.2 for an example.

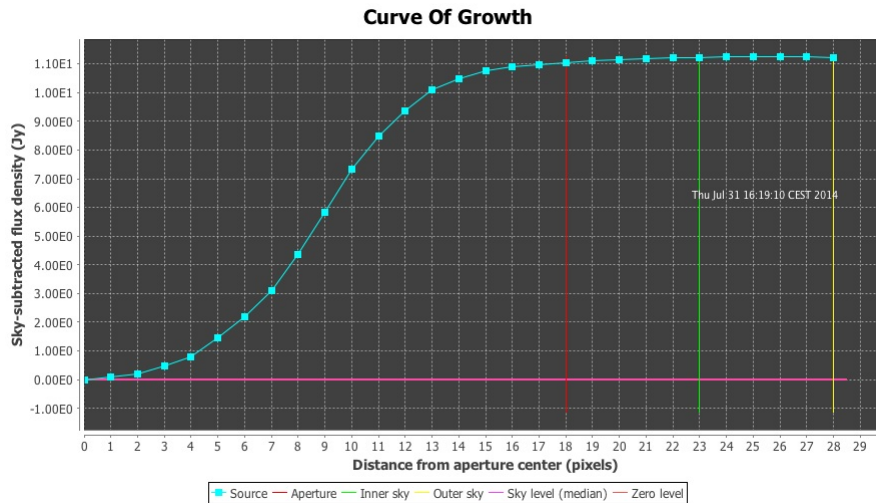


Figure 3.2: Curve of Growth for MN87 - 24  $\mu\text{m}$

Since the total flux measured from an aperture is the sum of the flux from the object and the sky, sky background measurements are needed to obtain meaningful photometry. For the sky background measurements, the sky annulus was set in a way that is distant from the central star to avoid any contribution from the source to the sky background estimates, has more pixels than the source aperture to have reliable statistics, and avoids bright stars that might fall within the annulus to avoid contamination of background sources. The dimensions

of the sky annulus (inner and outer radii) were chosen to be small enough to constrict the calculations to the local source, however, large enough to contain enough pixels counts to minimize the uncertainty of the source flux.

The size of the sky annulus was not fixed while determining the sky background calculations for the same object in the different bands; since the Point Spread Function (PSF) which is the 2D distribution of light in the focal plane of the telescope differs from one instrument to another. The great majority of the sky annulus pixels were purely background sky, however in some cases, the sky annulus contained one or two other bright objects. In this respect, I 'zapped' the pixels of the sky sources to exclude their effects from the sky-background calculations (ex: MN27 24  $\mu\text{m}$  in 3.6a ).

For the source photometry calculations, I've chosen the "No Aperture Interpolation" model (Model 0 in APT). This model would underestimate the intensity of the source only in the case where a large number of blank pixels exist in the aperture. Since none of my target apertures contained blank pixels, Model 0 was best fit for the photometric calculations of the source flux densities.

For the sky background calculations, the background level was determined by the median of all pixels in the sky annulus (Model B in APT). The median multiplied by the number of pixels in the aperture forms a product that is the sky contribution. The sky-subtracted source flux density is then calculated as the sum of the pixel values of the source aperture minus the background level subtracted from each pixel. For extended sources, the sky-median (Model B in APT) photometry is preferred over the sky-average (Model D in APT) photometry since the former is less influenced cosmic rays and 'hot' pixels. Hot pixels appear brighter than the surrounding pixels and arise due to the CCD sensors operating high rates of charges during long imaging exposures.

Following the above mentioned procedure, the sky-subtracted source flux densities were obtained. The uncertainties (errors) in the photometry were derived simultaneously to the process of the flux measurement in each individual band. APT computes the source-intensity uncertainty,  $\sigma_{src}$ , using:

$$\sigma_{src} = \sqrt{\frac{F_{src}}{\eta G N_{depth}} + A_{src} \sigma_{sky}^2 + \frac{\kappa (A_{src} \sigma_{sky})^2}{A_{sky}}} \quad (3.10)$$

where:

$F_{src}$  is the sky-background-subtracted source flux density or source intensity,  $G$  is the detector gain,  $N_{depth}$  is the depth of the coverage,  $\eta$  is the conversion factor from image data units to Data Number,  $A_{src}$  is the aperture area (in  $pixels^2$ ),  $\sigma_{sky}$  is the sky-background standard deviation (per pixel),  $\kappa$  is a factor that

depends on the optional background-estimation type or sky model employed in computation, and  $A_{sky}$  is the area of the sky annulus (in  $pixels^2$ ).

### 3.6.3 PACS-160 $\mu m$ and SPIRE-250 $\mu m$ Aperture Photometry

The majority of the PACS and SPIRE images reveal very strong and inhomogeneous cirrus emission that sometimes align with the target sources and thus make it difficult to measure a reliable flux.

The 160  $\mu m$  and 250  $\mu m$  maps of the five targets are mostly contaminated by this cirrus diffuse emission across all spatial scales. As a result, almost all of the sources in the images were not detected by the eye except for:

- GAL024.73+00.69 of the 160  $\mu m$  band
- WR31a of the 160  $\mu m$  band
- MN111 of the 250  $\mu m$  band

Contrary to the Curve of Growth plots for the 24  $\mu m$  and 70  $\mu m$ , those of the 160  $\mu m$  and 250  $\mu m$  bands do not saturate after a given radius, but clearly show the contribution of the background features, 3.3 for an example.

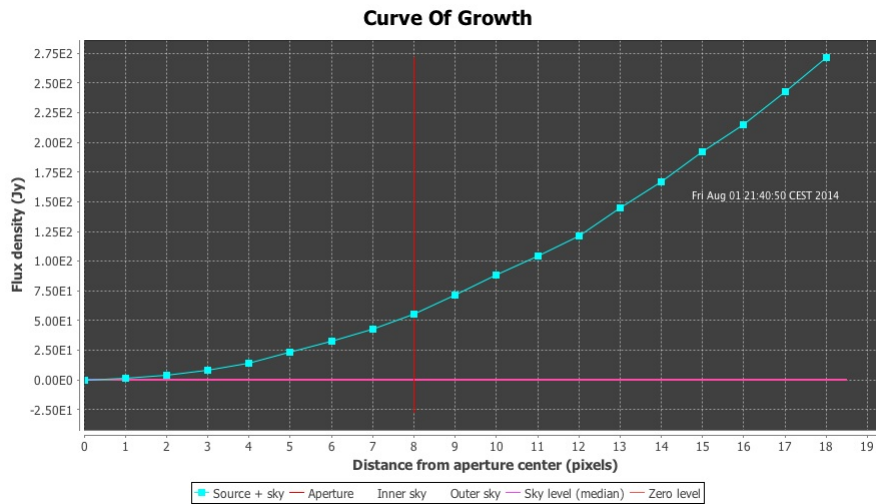


Figure 3.3: Curve of Growth for WR31a - 250  $\mu m$

On this account, the photometry approach adopted in 3.6.2 cannot be applied for the measurement of the flux densities of the 160- and 250  $\mu m$  sources and an important issue is then how to estimate the flux densities of the objects and the contribution of the diffuse background at the source position.

Therefore, to measure the flux of the target source, I placed an aperture at the given position of the source and computed the photometry by using the "No sky-background subtraction" (Model A in APT) which does not take into consideration the sky background contribution. To measure the sky background, I placed seven apertures around and close to the position of the source. The sky background value produced is per pixel and it is from a default annulus set by APT. I calculated the average sky background value of the seven apertures placed and multiplied it by the number of pixels in the source aperture. I then subtracted this value from the measured flux obtained from the central aperture of the target source. By this, I was able to estimate the real source flux.

$$F_s(\nu) = I - S \times N_{pix} \quad (3.11)$$

where  $F_s(\nu)$  is the real flux source,  $I$  is the non-sky-subtracted source flux,  $S$  is the average value of the sky background, and  $N_{pix}$  is the number of pixels within the source aperture.

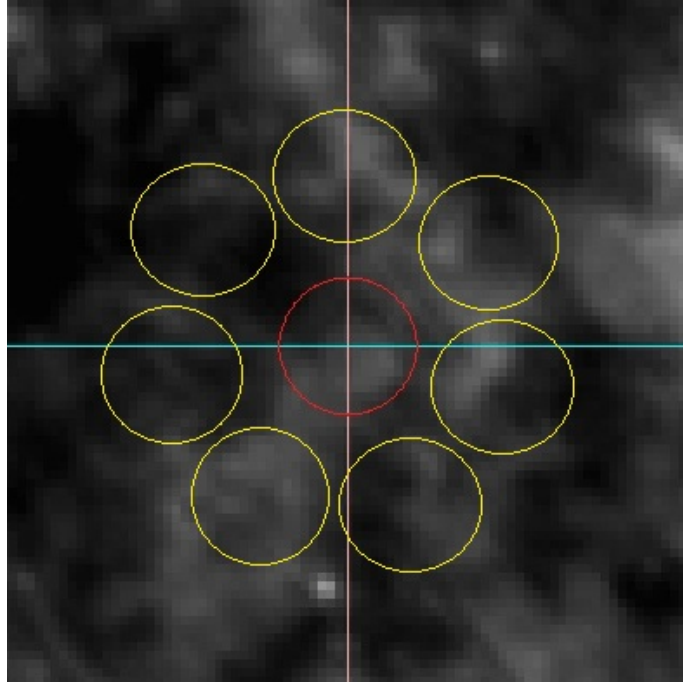


Figure 3.4: An interpretation for the aperture photometry done on MN87-160  $\mu\text{m}$

I also derived an upper limit for the undetected sources that is determined by:

$$S_{limit(\lambda)} = 3 \times err_{sky} \quad (3.12)$$

where:

$$err_{sky} = \sigma_{sky} \times N_{pix} \quad (3.13)$$

$\sigma_{sky}$  is the uncertainty of the background that arises from large scale features, for example, the cirrus emission evident in the 160 and 250  $\mu\text{m}$  maps. To determine the  $\sigma_{sky}$  value in eq.3.13, I placed seven apertures around the source in the image (in the same manner as previously described in this section), and calculated the average value of the standard deviation from each aperture. This average value is  $\sigma_{sky}$ .

In this way, we can conclude that any source with a flux  $\geq 3 \times err_{sky}$  should have been detected and so I assumed  $S_{limit(\lambda)}$  an upper limit at wavelength  $\lambda$  for the undetected objects. The  $3\sigma$  detection limit for the 5 objects are found in table 3.2.

Table 3.1: Flux densities of the sample obtained by photometry.

Name	$F_{\nu}(24\mu\text{m})$ (Jy)	$F_{\nu}(70\mu\text{m})$ (Jy)	$F_{\nu}(160\mu\text{m})$ (Jy)	$F_{\nu}(250\mu\text{m})$ (Jy)
-				
MN27	$1.38 \pm 0.01$	$12.90 \pm 3.6$	$5.57 \pm 5.56$	$9.41 \pm 9.41$
MN87	$11.06 \pm 0.02$	$29.82 \pm 5.46$	$7.65 \pm 7.65$	$13.12 \pm 13.1$
MN111	$5.93 \pm 0.01$	$80.62 \pm 8.98$	$88.06 \pm 88.06$	$45.01 \pm 0.66$
WR31a	$16.73 \pm 0.02$	$29.75 \pm 5.47$	$10.49 \pm 3.26$	$0.78 \pm 0.78$
GAL024.73	$10.24 \pm 0.03$	$56.88 \pm 7.6$	$-3.85 \pm 3.85$	$-11.53 \pm 11.53$

The negative values are a result of manually subtracting the high background flux from the source flux. In reality, the source intensities are 0Jy. They are undetected. When plotting, for the sake of simplicity, they were set to 0Jy.

Table 3.2:  $3\sigma$  detection limit.

Name	$\lambda$ ( $\mu\text{m}$ )	$S_{limit(\lambda)}$ (Jy)
-		
MN27	160	33.4
	250	19
MN87	160	55.8
	250	40.7
MN111	160	157.5
WR31a	250	38.1
GAL024.73	250	36.8

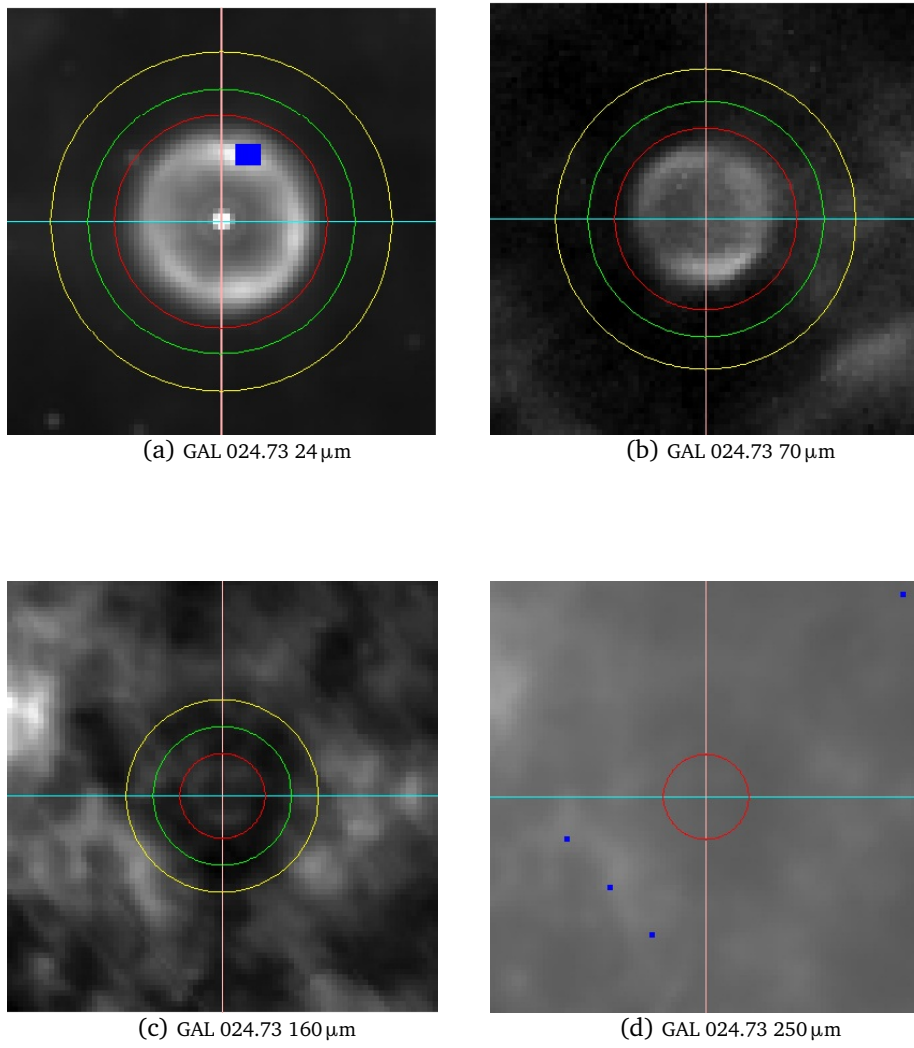


Figure 3.5: GAL 024.73+00.69 aperture photometry.

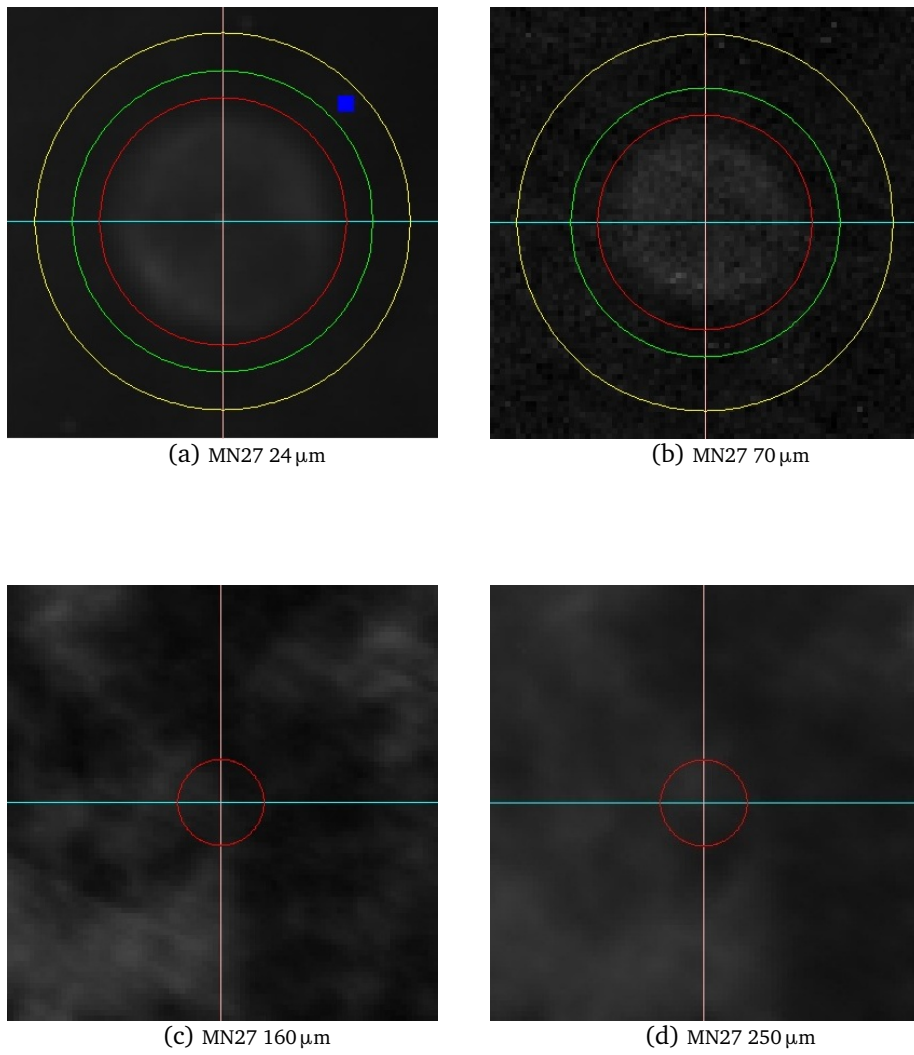


Figure 3.6: MN27 aperture photometry.

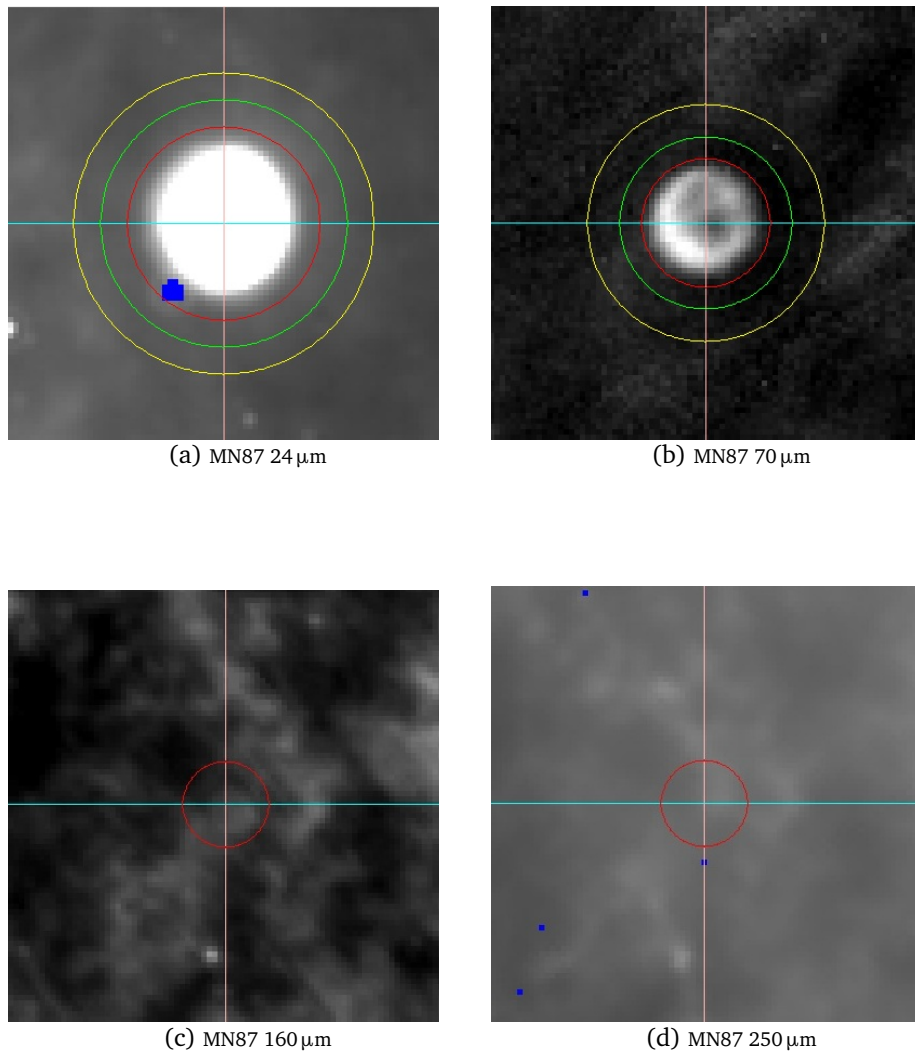


Figure 3.7: MN87 aperture photometry.

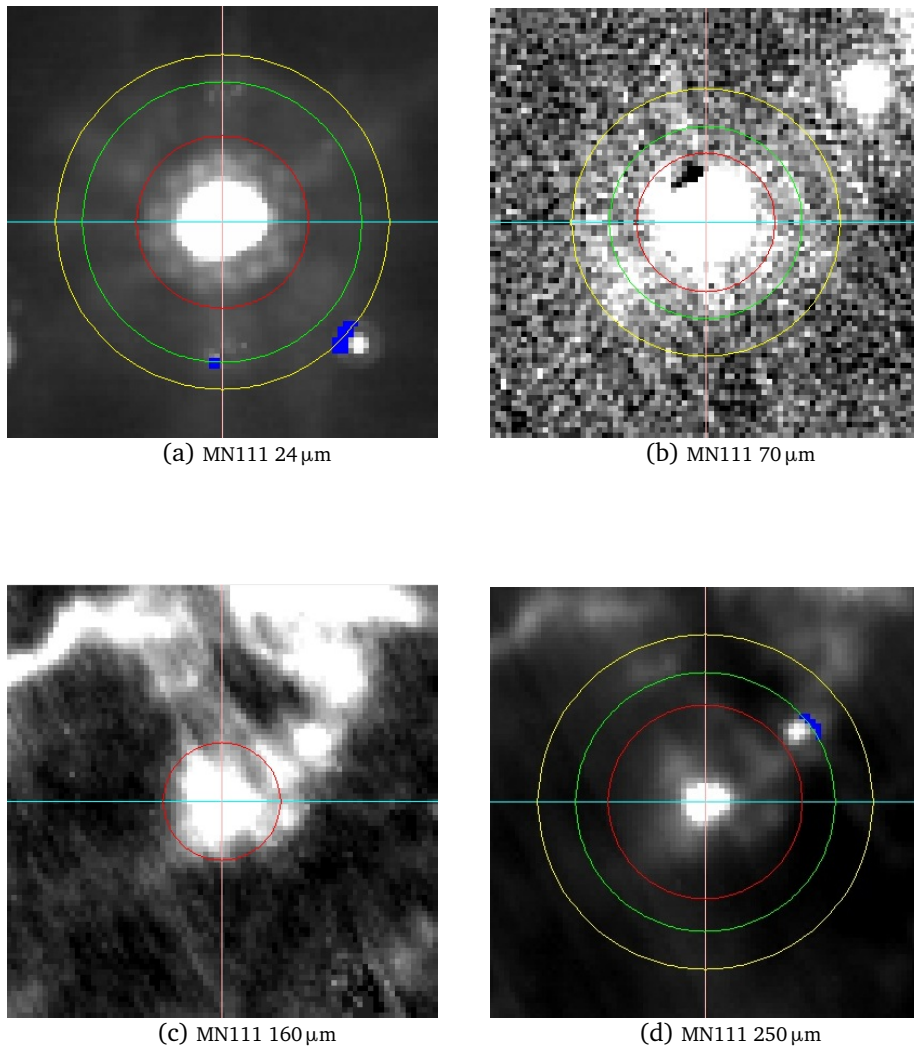


Figure 3.8: MN111 aperture photometry.

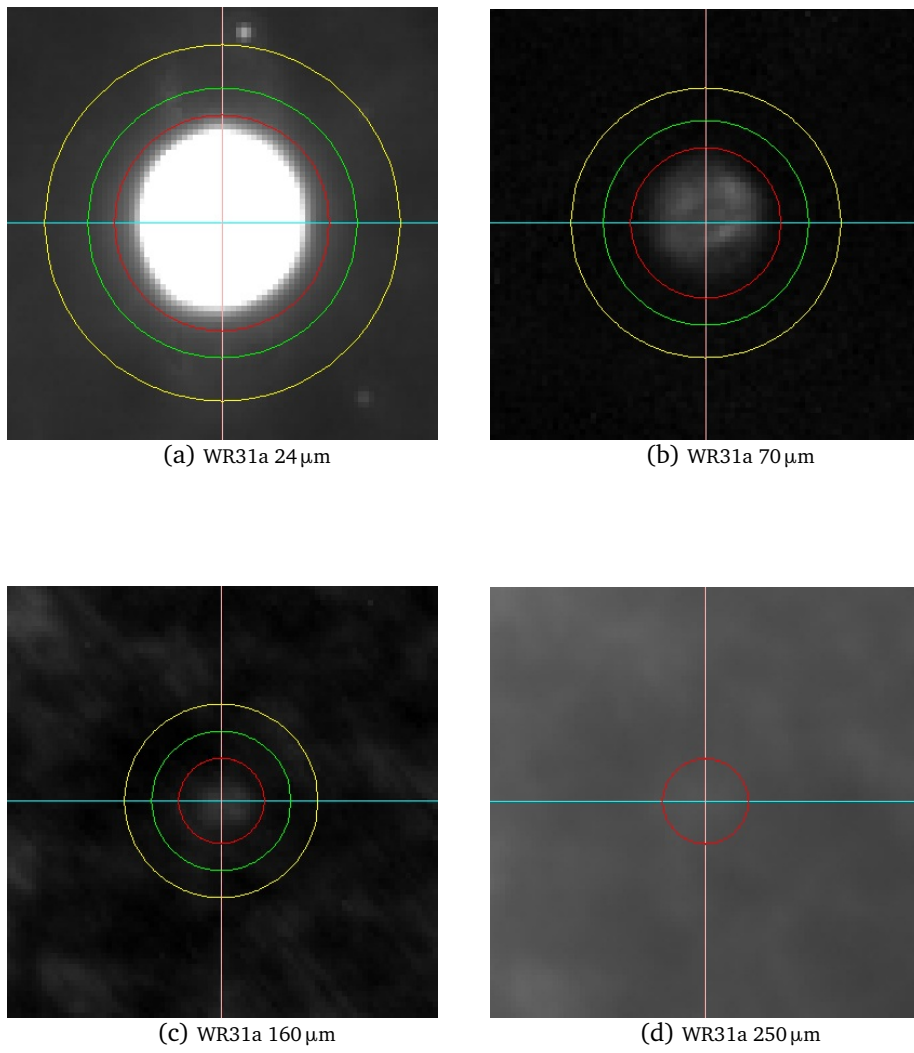


Figure 3.9: WR31a aperture photometry.



# Chapter 4

## Results and Discussion

### 4.1 Dust Temperature

Assuming the dust distribution is optically thin at all wavelengths so as the radiation emitted by the dust shell is not attenuated by the absorption due to the dust opacity, the dust temperature  $T_d$  can then be determined by fitting the observed fluxes to a modified blackbody (MBB).

For the SED fitting, I modelled each set of the 24, 70, 160 and 250  $\mu\text{m}$  data of the 5 objects with an MBB of the form:

$$F_\nu(\lambda) = A \frac{2hc^2}{\lambda^5} \frac{1}{e^{(hc/\lambda kT_d)} - 1} \times \left(\frac{\lambda_0}{\lambda}\right)^\beta \quad (4.1)$$

Where  $T_d$  is the unknown parameter,  $F(\nu)$  is the flux emitted by a blackbody at  $T_d$ ,  $A$  is the normalization parameter that normalizes the SED with respect to the data points,  $\beta$  is the grain emissivity index, and  $\lambda_0 = 2\pi a$  can be regarded as the characteristic grain size where  $a = 0.1 \mu\text{m}$  is the assumed grain size. The size-distribution of dust grains varies. For circumstellar dust grains, it ranges from nanoparticles up to few-microns with a pronounced crowding for small sizes ( $a = 0.01 \mu\text{m}, \dots 0.1 \mu\text{m}$ ) Gail and Sedlmayr (2013).

However, the choice for  $\lambda_0$  needs to be explained. Dust grains are inefficient radiators at long wavelengths and favor absorbing and emitting radiation with wavelengths smaller than their size. The extinction efficiency ( $Q_{ext}$ ) can be written in terms of the scattering and absorption efficiency as:

$$Q_{ext} = Q_{scat} + Q_{abs} \quad (4.2)$$

with the scattering term expressed in terms of the **grain albedo**,  $\omega$ :

$$\omega = \frac{Q_{scat}}{Q_{abs}} \quad (4.3)$$

where  $\omega = 1$  for a perfectly-scattering grain, while  $\omega = 0$  for a perfectly-absorbing grain.

For a given dust grain, the emitting efficiency for a perfectly-absorbing grain:

$$\epsilon = 1 - \omega \approx 1 \quad (4.4)$$

A relation between the size grain and the wavelength of the incident light is can be expressed as:

$$x = \frac{2\pi a}{\lambda_0} \quad (4.5)$$

where for a strongly-absorbing grain ( $a \gg \lambda_0$ ),  $x = \frac{2\pi a}{\lambda_0} > 1$  and thus we can consider the limit for a perfectly-absorbing dust grain as:  $\lambda_0 \approx 2\pi a$  Backman and Paresce (1993).

The best-fit model was obtained by performing a non-linear least squares fitting minimization based on the Levenberg - Marquardt (LM) method (Lourakis (2005)). I took the uncertainties of the flux measurements into account to weight the data during the procedure. The weighting (where certain data points factor more heavily than others into the fitting) goes as  $1/error^2$ . This way the fit tends to the points of least errors.

The dust grains hold varied properties (size, shape, composition) along the line of sight where the temperature of the dust may significantly vary depending on these properties. Therefore, to derive an estimate of the dust  $T_d$ , I considered models with different emissivity index values  $\approx 1 \leq \beta \leq 2$ . I decided to fix the values at  $\beta = 1$ ,  $\beta = 1.5$ , and  $\beta = 2$  at derive the dust temperature at each.

The fitting plots for each object are found in Fig 4.1, 4.2, 4.3,4.4 and 4.5.

Table 4.1 shows the best-fit values of  $T_d$  :

While performing aperture photometry, the contribution of the star was not excluded, i.e. the star was included in the aperture, and the flux densities were derived according to that. Ideally, a two-component model would have yielded much precise results for the derivation of the dust temperatures. A two-component model describes the source as: the central star whose emission

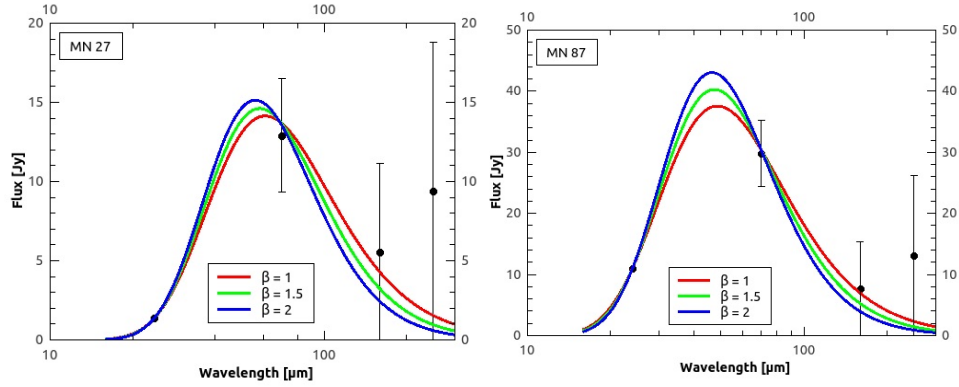


Figure 4.1: MBB fit to the MN27 emission. Figure 4.2: MBB fit to the MN87 emission.

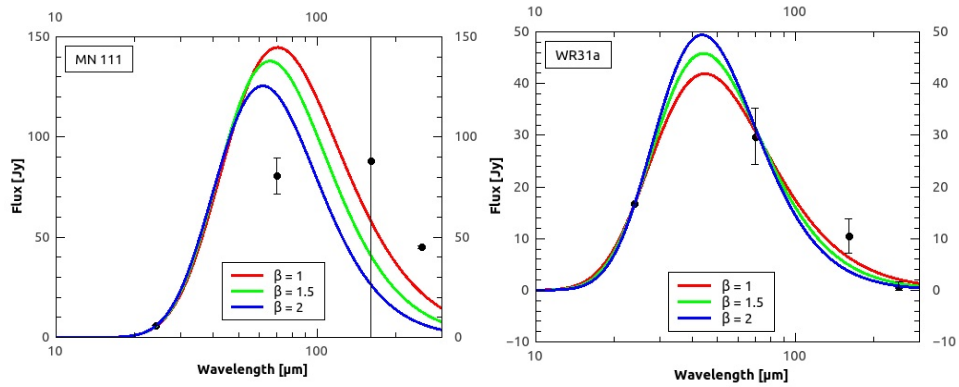


Figure 4.3: MBB fit to the MN111 emission. Figure 4.4: MBB fit to the WR31a emission.

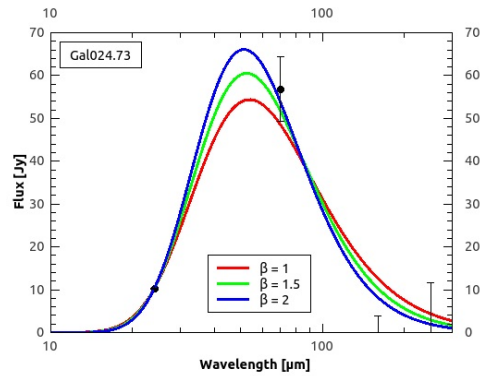


Figure 4.5: MBB fit to the GAL024.73+00.69 emission

Table 4.1: Best-fit  $T_d$  values.

Name	$\beta$	$T_d$ (K)
-		
MN27	1	$60 \pm 2.7$
	1.5	$55.5 \pm 2.6$
	2	$51.6 \pm 2.5$
MN87	1	$75.3 \pm 2.4$
	1.5	$68 \pm 2$
	2	$62.2 \pm 2$
MN111	1	$52 \pm 4.5$
	1.5	$49 \pm 5.4$
	2	$47 \pm 6.1$
WR31a	1	$82 \pm 2.5$
	1.5	$73 \pm 2.3$
	2	$66.3 \pm 2.2$
GAL024.73	1	$68 \pm 3.32$
	1.5	$61.5 \pm 2$
	2	$56.4 \pm 1.3$

is modelled with a blackbody, embedded in a dusty envelope whose emission is modelled with a greybody.

$$F_{nu} \approx B_{\lambda}(T_b) + B_{\lambda}(T_d) \times Q(\lambda) \quad (4.6)$$

where  $B_{\lambda}(T_b)$  is the blackbody emission of the star at wavelength  $\lambda$  and  $T_b$  is the effective temperature of the central star.

However, at the shortest wavelengths, the energy distribution is approximately only that of the star, i.e. the dust does not contribute at the shortest wavelengths. The dust absorbs the shortest-wavelength radiation and emits it in the IR wavelengths, the radiation emitted is that of the dust. Thus the consideration that I have taken in this thesis, that is, to model the data to a greybody only is fairly in place as well.

The peak of dust energy distribution is determined by the dust effective temperature. From the plots 4.1, we see that the SEDs peak are at approximately the same wavelength range which implies that the objects in the sample have the same dust temperatures range ( $\approx 50 - 80$  K).

The choice of  $\beta$  clearly affects the effective temperature of the dust. The anti-

correlation between  $T_d$  and  $\beta$  is shown in table 4.1. The derived  $T_d$  for all five objects follow the same decreasing trend for increasing  $\beta$  values. The anti-correlation is present for all objects regardless of their type. This is also seen in the dust energy distribution at wavelengths further away from the peak, the slope of the dust SEDs is affected by the choice of  $\beta$ . As we assumed different  $\beta$  values for different grain composition and provided that we assumed that the grain size distribution is not changed, the values confirm that the chemical composition of the grains have a direct influence on their temperature.

On the other hand, there is a certain degeneracy between  $\beta$  and  $T_d$ . We expect higher temperatures to shift the peak of the SED towards shorter wavelengths. However, as seen from 4.1, there is a slight discrepancy in the results; SEDs with higher temperatures (red curves of  $\beta = 1$ ) are shifted towards the longer wavelengths as opposed to SEDs with the lower temperatures (blue curves of  $\beta = 2$ ). This is a consequence of the normalization parameter  $A$ . Physically, the overall effect of  $A$  depends on the dust mass and the emissivity. The more dust mass and the more emission, the greater the normalization needed to obtain a reasonable fit (and vice versa). A change in the value of  $A$  also moves the SED horizontally. This explains why we see such degeneracy in the plots. The higher the temperature, the more light energy emitted, and thus the higher the peak of the SED, and so the greater the normalization value that produces an appropriate fit, and hence the greater the horizontal shift. Therefore, the peak value and peak position are strongly affected by the normalization parameter.

## 4.2 Dust Mass

$M_d$  was calculated for only two objects of the original sample. The dust mass equation (eq. 4.7) depends on the distance  $D$  to the object. Given that no resources were available during the time of this thesis that contained information about the distances to the other three objects, I restricted the estimation of  $M_d$  to only WR31a (WR star) and GAL024.73+00.69 (LBV star) of known distances.

Using the flux densities,  $M_d$  was estimated by:

$$M_d = \frac{F(\nu)D^2}{B_\lambda(T_d)\kappa_d} \quad (4.7)$$

where:

$M_d$ , the dust mass, in  $M_\odot$ .

$T_d$ , the effective dust temperature derived from the MBB fits, in  $K$  (see table 4.1).

$D$ , the distance to the object, in  $m$ .

$F(\nu)$ , the observed flux densities, in Jy.

$B_\lambda(T_d)$ , the Planck function converted to units of Jy using the relation:

$$F(\nu) = B_\lambda(T_d) \times 10^{26} \times \frac{\lambda^2}{c}$$

$\kappa_d$ , the grain mass absorption coefficient, in  $m^2/kg$ , given by:

$$\kappa_d = \frac{3}{4\rho} \frac{Q(\lambda)}{a} \quad (4.8)$$

In this work, I explored three possible dust compositions for spherical grains of radius  $a$ ; amorphous carbon (Rouleau and Martin (1991)), silicates (Li and Draine (2001)), and an assumed mixture of both.

To derive values for  $\kappa_d$ , determination of  $\frac{Q(\lambda)}{a}$  must be made. In the long-wavelength regime (Rayleigh-limit), the absorption effects always dominate those of scattering (Krugel (2002)) and so to derive the emissivity term, I made use of the extinction efficiency curve to derive the values of  $\frac{Q(\lambda)}{a}$  at  $70 \mu m$  where the emission of the 2 objects peaked (see fig. 4.6). I lifted a perpendicular whose length is determined by the intersection with the curve representing the grain composition, and found its corresponding point at the vertical axis.

This yielded values of  $\frac{Q(\lambda)}{a} = 300, 800$  and  $500 \text{ cm}^{-1}$  for amorphous carbon, silicates and the assumed mixed component respectively.

The mass density is  $\rho_{\text{amc}} = 1.8 \text{ gcm}^{-3}$  for amorphous carbon,  $\rho_s = 3.3 \text{ gcm}^{-3}$  for silicates and an assumed  $\rho_m = 2.6 \text{ gcm}^{-3}$  for the mixed component. Plugging the mass density values for the different compositions and their respective  $\frac{Q(\lambda)}{a}$  values in eq. 4.8 gave  $\kappa$  values shown in table 4.2 ( where:  $\kappa_c$  for the amorphous carbon dust,  $\kappa_s$  for the silicate dust, and  $\kappa_m$  for the mixed component dust.)

The distance is 5.2kpc to GAL024.73+00.69 (Petriella et al. (2011)) and 8000pc to WR31a (van der Hucht (2001)).

Table 4.2:  $\kappa$  values for the different species.

Name	$\kappa$ ( $m^2/kg$ )
-	
Amorphous Carbon	12.5
Silicates	18.18
Mixed	14.42

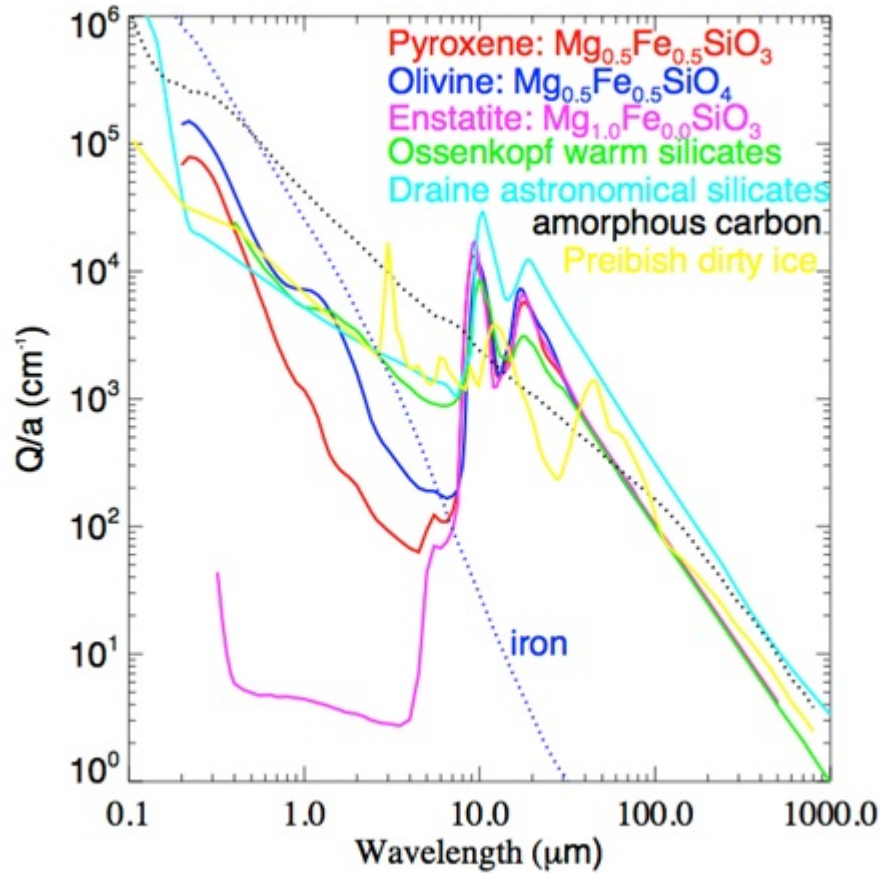


Figure 4.6: Calculated extinction efficiency,  $Q_{ext}$ , over particle radius,  $a$ , in the Rayleigh-limit for different types of silicates Dorschner et al. (1995), Jäger et al. (2003). For comparison pure iron and amorphous carbon (cel 1000) from Jäger et al. (1998) are shown. Notice that at 24  $\mu\text{m}$  and longer wavelengths the difference between the different dust type is less significant than for the shorter wavelengths.

Plugging the values of the different parameters in eq. 4.7 returned approximate estimates of  $M_d$  given in tables 4.3, 4.4, 4.5, 4.6, 4.7, and 4.8. These values represent the amount of dust deposited per one episode of ejection given an assumed composition.

Table 4.3: Dust mass estimate for WR31a for  $\kappa_c$ 

$\beta$	$T$ (K)	$\kappa_c$ ( $m^2/kg$ )	$M_d$ ( $M_\odot$ )
-			
1	82	12.5	0.007
1.5	73	12.5	0.01
2	66.3	12.5	0.013

Table 4.4: Dust mass estimate for WR31a for  $\kappa_s$ 

$\beta$	$T$ (K)	$\kappa_c$ ( $m^2/kg$ )	$M_d$ ( $M_\odot$ )
-			
1	82	18.18	0.005
1.5	73	18.18	0.007
2	66.3	18.18	0.009

Table 4.5: Dust mass estimate for WR31a for  $\kappa_M$ 

$\beta$	$T$ (K)	$\kappa_c$ ( $m^2/kg$ )	$M_d$ ( $M_\odot$ )
-			
1	82	14.42	0.006
1.5	73	14.42	0.008
2	66.3	14.42	0.01

Table 4.6: Dust mass estimate for GAL024.73+00.69 for  $\kappa_c$ 

$\beta$	$T$ (K)	$\kappa_c$ ( $m^2/kg$ )	$M_d$ ( $M_\odot$ )
-			
1	68	12.5	0.01
1.5	61.52	12.5	0.014
2	56.4	12.5	0.02

Table 4.7: Dust mass estimate for GAL024.73+00.69 for  $\kappa_s$ 

$\beta$	$T$ (K)	$\kappa_c$ ( $m^2/kg$ )	$M_d$ ( $M_\odot$ )
-			
1	68	18.18	0.007
1.5	61.52	18.18	0.009
2	56.4	18.18	0.01

Table 4.8: Dust mass estimate for GAL024.73+00.69 with  $\kappa_M$ 

$\beta$	$T$ (K)	$\kappa_c$ ( $m^2/kg$ )	$M_d$ ( $M_\odot$ )
-			
1	68	14.42	0.008
1.5	61.52	14.42	0.012
2	56.4	14.42	0.016

We see that for GAL024.73+00.69, the amorphous carbon average dust mass of  $0.014M_{\odot}$  is insignificantly greater than that of the mixed-component of  $0.012M_{\odot}$  which in turn is greater than that of the silicate dust of  $0.008M_{\odot}$ .

However, for the case of WR31a, the average silicate dust mass of  $0.02M_{\odot}$  is greater than that of the mixed component of  $0.008M_{\odot}$  which is slightly greater than that of the amorphous carbon dust of  $0.007M_{\odot}$ .

However, it is worthy to note that the composition of the deposited dust and how much of it is injected into the ISM depends on which evolutionary stage the star is in and thus what products of nuclear fusion appear on the surface to be deposited. Different parameters may affect the chemical composition of the ejected nebulae, for example mixing with swept-up gas of previously blown material and chemical mixing due to the rotation of the star. The  $M_d$  values for each object in this thesis mainly looks into how much dust mass of different composition is injected into the ISM.

On the other hand, comparing the amount of mass ejected from the two stars of the same chemical composition, we find that those associated with GAL024.73+00.69 are greater than that of WR31a which may be consistent with the belief that LBVs are the major contributors of circumstellar material.

It is important not to over interpret the dust mass results derived in this thesis as the values depend on various educated guesses. The uncertainty in the parameters will inevitably result in the uncertainty of the  $M_d$  results.



# Chapter 5

## Summary and Conclusion

One main question of interest in this thesis was to estimate how much mass a massive star returns to the interstellar medium at the late stages of its evolution.

I have investigated the dust emission of a sample selected from Gvaramadze et al. (2010). At the beginning of this thesis, I had expected to identify a circumstellar dust at mid-IR wavelengths associated with warm dust and a shell at longer far-IR wavelengths associated with cold dust which may infer that the massive star has experienced an episode of mass ejection which was collected into a shell and is expanding into the interstellar medium. However, visual inspection of the objects, mainly by RGB color maps and intensity contours, revealed that most of the cold dust emission is drowned by warm dust emission at 24 and 70  $\mu\text{m}$ . I deduced that there is a possibility the material ejected had been followed by a successive episode of ejection in which way the cold and warm dust overlapped. Another possibility is that the shell of circumstellar material may have been expelled a long time ago, has since expanded further and further and has dispersed into the interstellar medium.

Performing aperture photometry on a sample of 5 morphologically-interesting objects (MN27, MN87, MN111, GAL024.73+00.69, and WR31a) yielded flux density measurements for each object at four bands centered at 24, 70, 160 and 250  $\mu\text{m}$ . For undetected sources at far-IR wavelengths, the challenge laid in determining the background that was dominated by cirrus emission and so was one of the main uncertainties in deriving the fluxes. The flux densities associated with far-IR wavelengths had error bars as high and low as the measured source flux.

To determine the dust shell effective temperature  $T_d$  of the 5 objects, I have concentrated on fitting the flux densities to a modified version of the blackbody for 3 different cases in which the emissivity power-law index was  $\beta = 1, 1.5$

and 2 for each. The derived  $T_d$  were in a range of 50 – 80 K at a wavelength peak 70  $\mu\text{m}$ . I noticed an anti-correlation between  $\beta$  and  $T_d$  which is not still well-understood due to the ambiguity of the nature of  $\beta$ . However, for both objects, when  $\beta = 2$ , the dust temperatures were colder and the dust masses were higher by a factor of 0.5 than for cases of  $\beta = 1$ . This could give indication about constraining the dust emissivity index when measuring parameters of cold dust.

I have estimated the dust masses associated with 2 objects, GAL024.73+00.69 and WR31a, from the 70  $\mu\text{m}$  fluxes and from the fitted temperatures for three different dust compositions, amorphous carbon dust, silicate dust, and an assumed mixed component of both. I concluded that GAL024.73+00.69 would expel a greater fraction if the dust was of amorphous carbon nature  $\approx 0.014M_\odot$ , while WR31a would expel a greater fraction if it was of silicate nature  $\approx 0.02M_\odot$ .

I had expected that the dust mass via stellar winds would account for a substantial fraction. However, that was not the case. Whether these types of stars expel a much significant amount of dust in later episodes before exploding into supernovae could be possible.

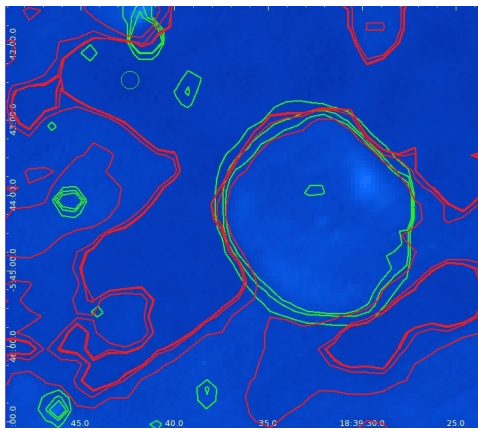
$\beta$  and  $\kappa$  are dependent on the properties of the dust grains such as composition, size and emissivity. A precise estimate of these values is necessary to accurately derive other properties of the observed object. By deriving accurate measurements of  $\beta$  and  $\kappa$ , we will be able to determine more reliable physical measures of the properties of the dust such as the temperatures and masses.

There are still more to explore in the subject treated in this thesis. In addition to what has been mentioned above, estimates and measurements of the distances to the other newly discovered objects in the Galactic disk would enable us to approximate the dust masses, temperatures and other properties of those circumstellar dust shells which have not been explored yet.

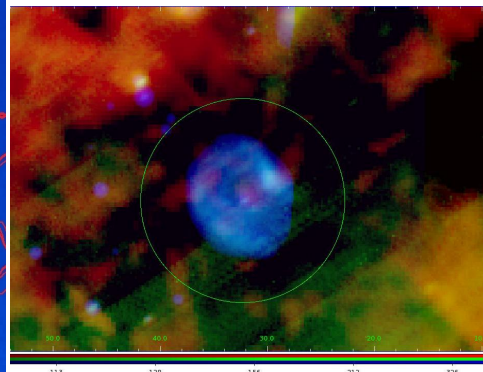


# Appendix A

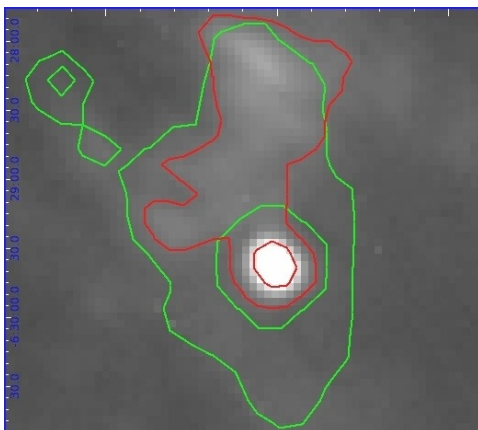
## Contoured and RGB Images



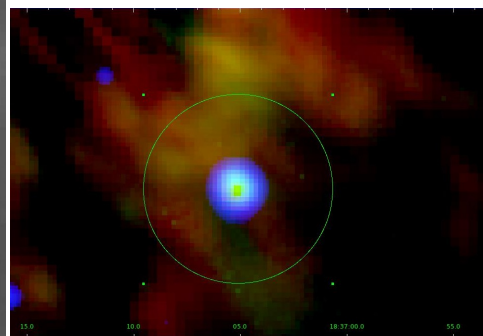
(a) GAL026.47+00.02: MIPS 24  $\mu\text{m}$  data (green contours) and PACS 70  $\mu\text{m}$  (red contours).



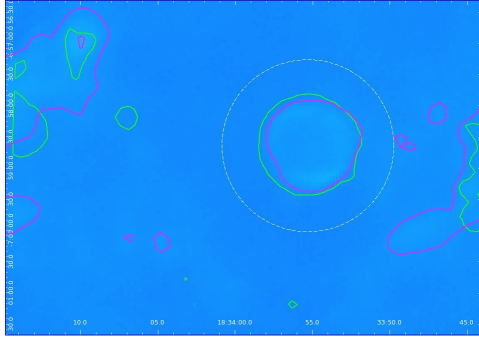
(b) GAL026 RGB



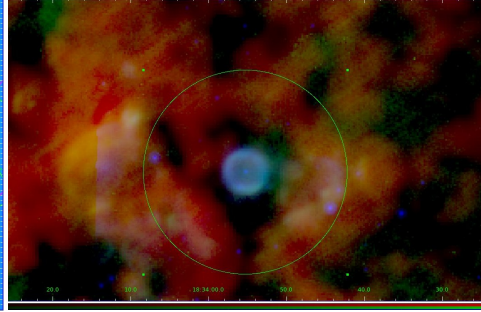
(a) GAL025+00.2: MIPS 24  $\mu\text{m}$  data (green contours) and PACS 70  $\mu\text{m}$  (red contours)



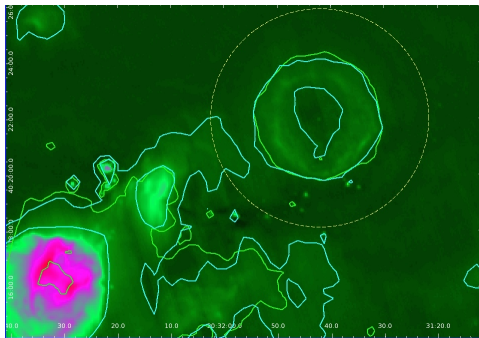
(b) GAL079 RGB



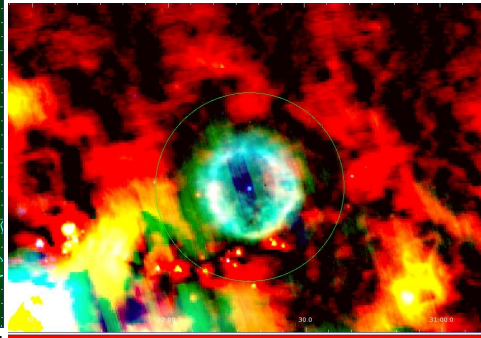
(a) GAL024.73+00.69: MIPS 24  $\mu\text{m}$  data (green contours) and PACS 70  $\mu\text{m}$  (magenta contours)



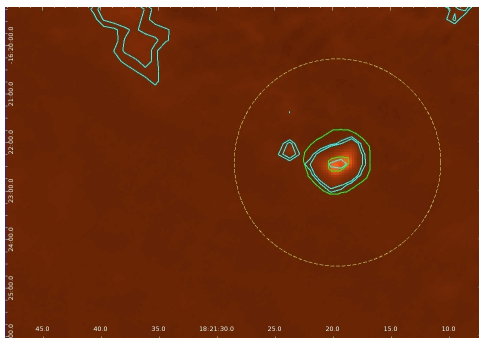
(b) GAL024 RGB



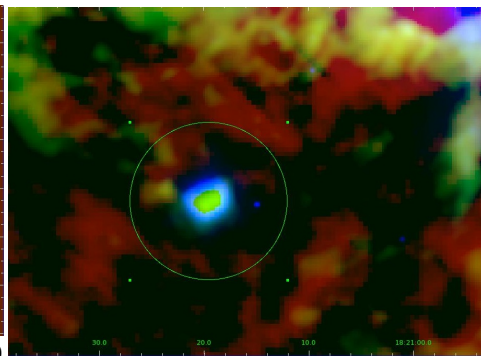
(a) GAL079: MIPS 24  $\mu\text{m}$  data (green contours) and PACS 70  $\mu\text{m}$  (cyan contours)



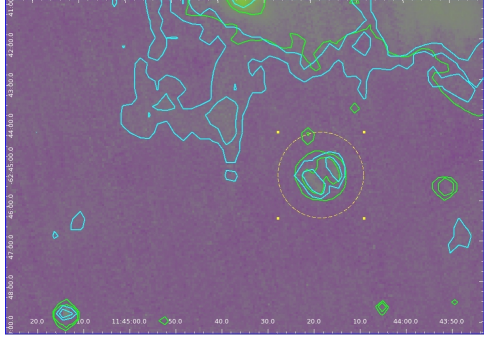
(b) GAL079 RGB



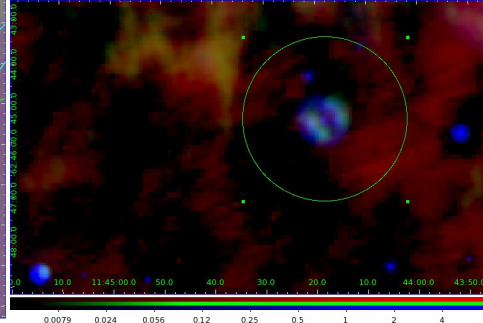
(a) HD168625: MIPS 24  $\mu\text{m}$  data (green contours) and PACS 70  $\mu\text{m}$  (cyan contours)



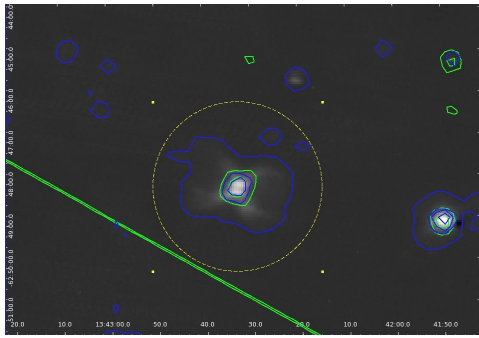
(b) HD168625 RGB



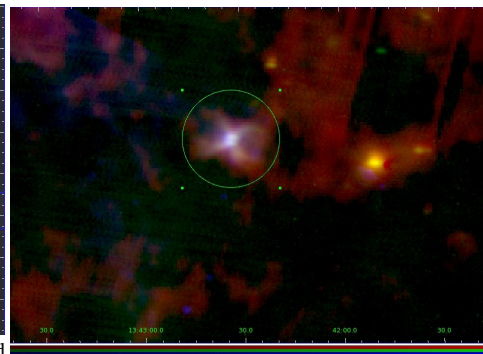
(a) MN1: MIPS 24  $\mu\text{m}$  data (green contours) and PACS 70  $\mu\text{m}$  (cyan contours)



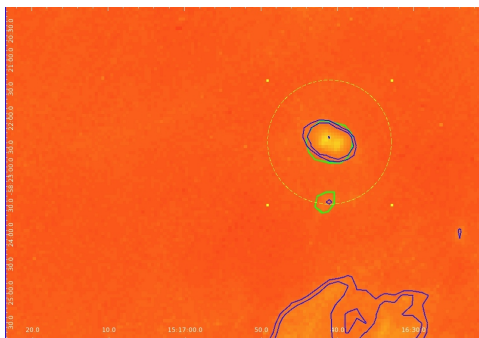
(b) MN1 RGB



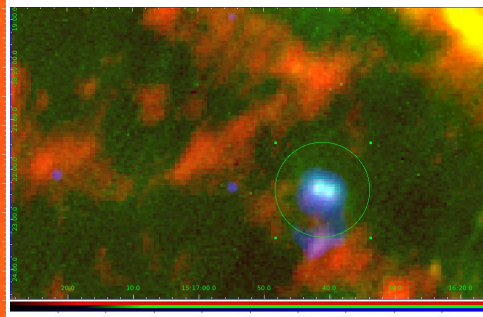
(a) MN13: MIPS 24  $\mu\text{m}$  data (green contours) and PACS 70  $\mu\text{m}$  (blue contours)



(b) MN13 RGB



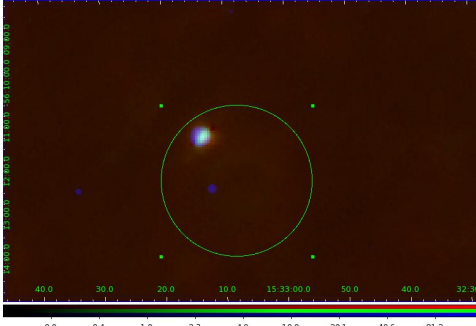
(a) MN18: MIPS 24  $\mu\text{m}$  data (green contours) and PACS 70  $\mu\text{m}$  (blue contours)



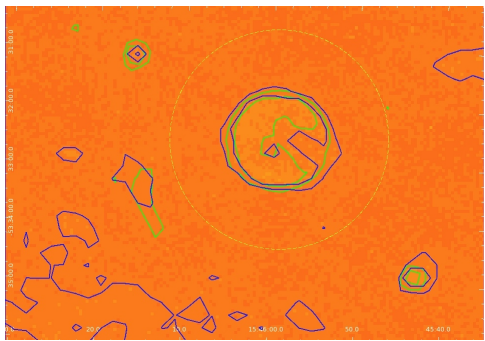
(b) MN18 RGB



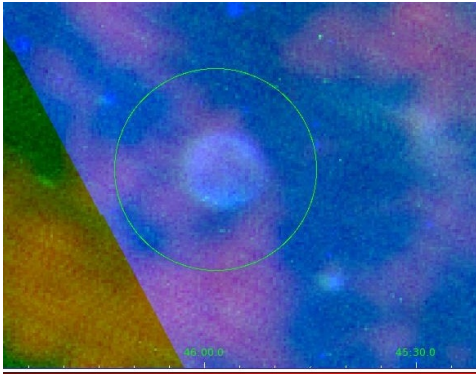
(a) MN21: MIPS 24  $\mu\text{m}$  data (green contours) and PACS 70  $\mu\text{m}$  (cyan contours)



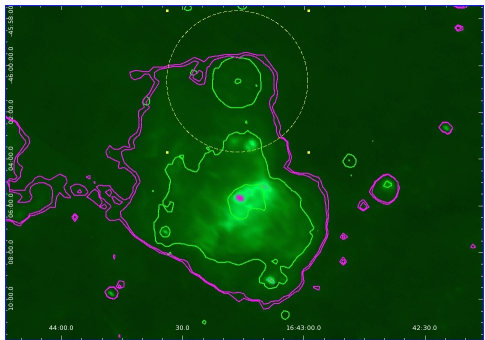
(b) MN21 RGB



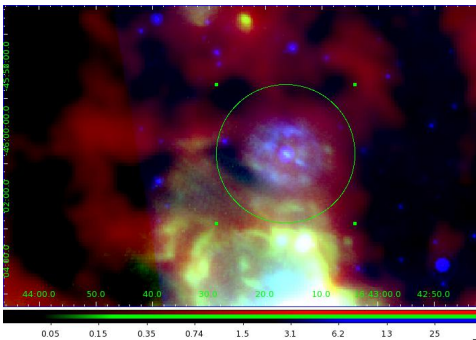
(a) MN27: MIPS 24  $\mu\text{m}$  data (green contours) and PACS 70  $\mu\text{m}$  (blue contours)



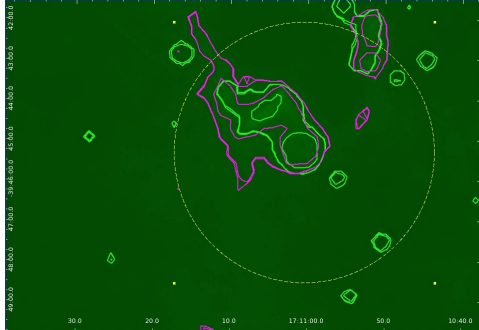
(b) MN27 RGB



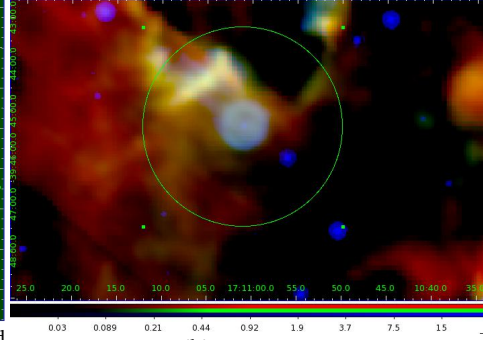
(a) MN46: MIPS 24  $\mu\text{m}$  data (green contours) and PACS 70  $\mu\text{m}$  (magenta contours)



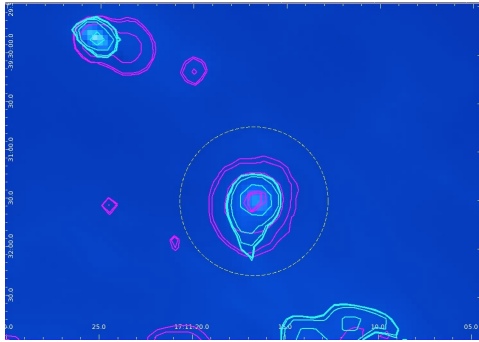
(b) MN46 RGB



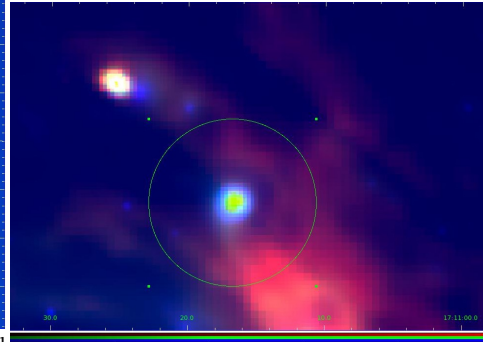
(a) MN55: MIPS 24  $\mu\text{m}$  data (green contours) and PACS 70  $\mu\text{m}$  (magenta contours)



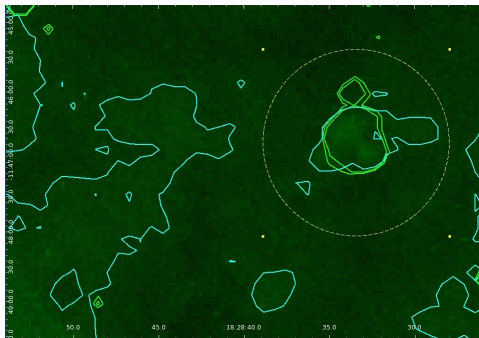
(b) MN55 RGB



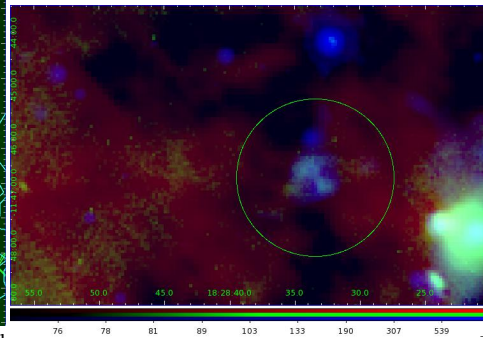
(a) MN56: MIPS 24  $\mu\text{m}$  data (magenta contours) and PACS 70  $\mu\text{m}$  (cyan contours)



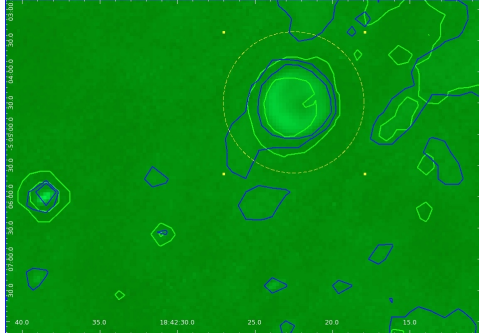
(b) MN56 RGB



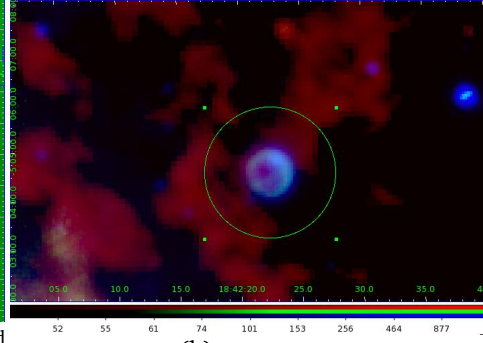
(a) MN79: MIPS 24  $\mu\text{m}$  data (green contours) and PACS 70  $\mu\text{m}$  (cyan contours)



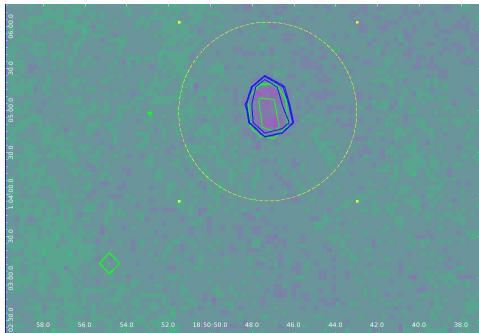
(b) MN79 RGB



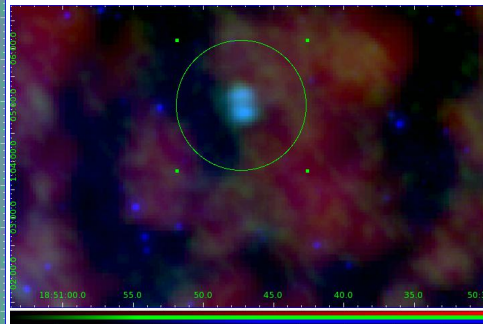
(a) MN87: MIPS 24  $\mu\text{m}$  data (green contours) and PACS 70  $\mu\text{m}$  (blue contours)



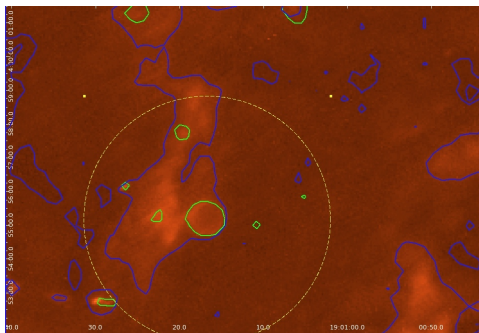
(b) MN87 RGB



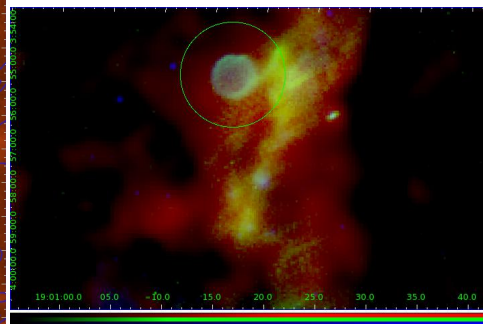
(a) MN94: MIPS 24  $\mu\text{m}$  data (green contours) and PACS 70  $\mu\text{m}$  (blue contours)



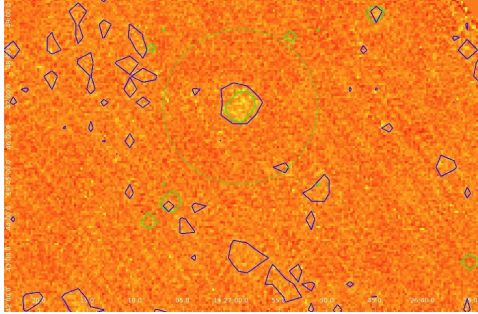
(b) MN94 RGB



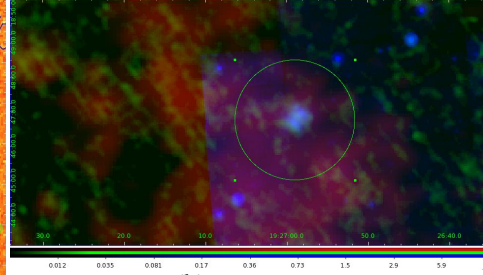
(a) MN98: MIPS 24  $\mu\text{m}$  data (green contours) and PACS 70  $\mu\text{m}$  (blue contours)



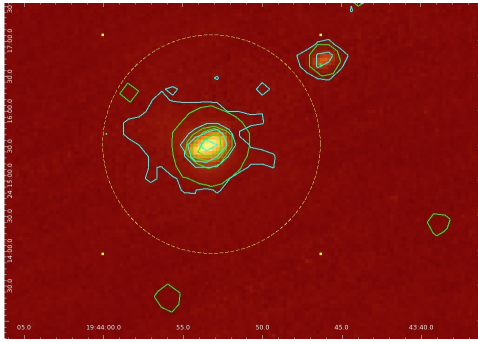
(b) MN98 RGB



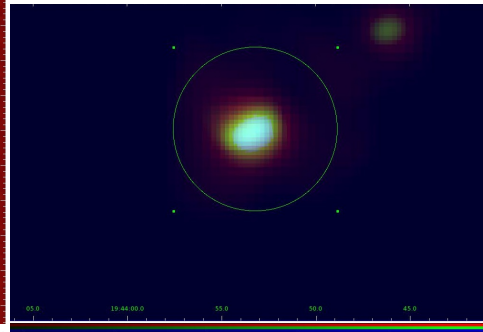
(a) MN108: MIPS 24  $\mu\text{m}$  data (green contours) and PACS 70  $\mu\text{m}$  (blue contours)



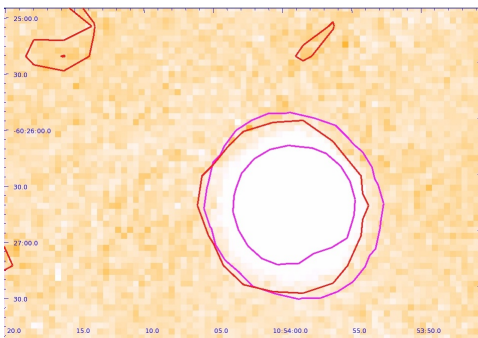
(b) MN108 RGB



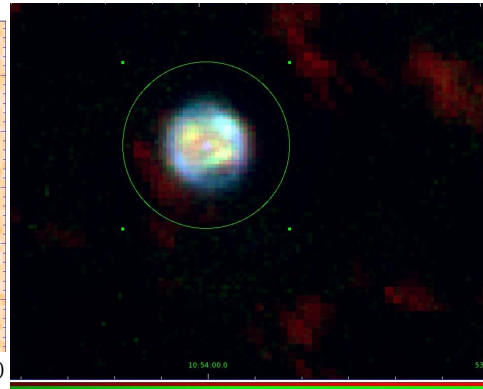
(a) MN111: MIPS 24  $\mu\text{m}$  data (green contours) and PACS 70  $\mu\text{m}$  (cyan contours)



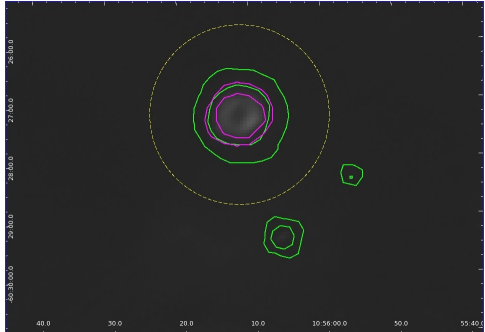
(b) MN111 RGB



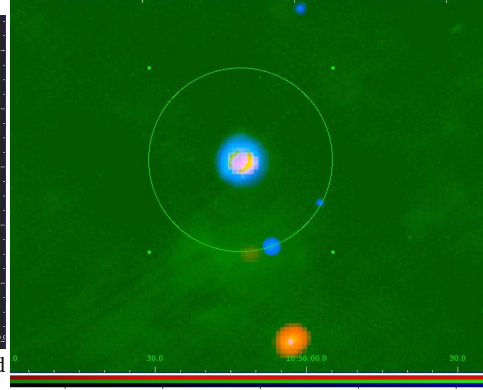
(a) WR31a: MIPS 24  $\mu\text{m}$  data (magenta contours) and PACS 70  $\mu\text{m}$  (red contours)



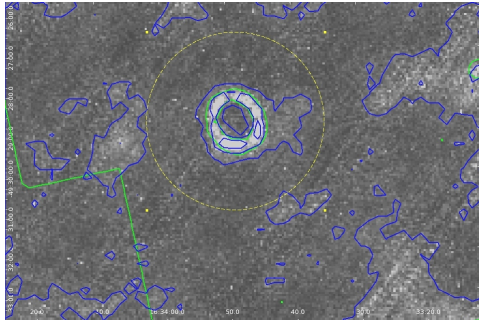
(b) WR31a RGB



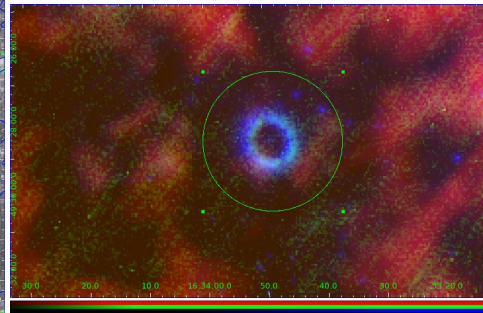
(a) WR31b: MIPS 24  $\mu\text{m}$  data (green contours) and PACS 70  $\mu\text{m}$  (magenta contours)



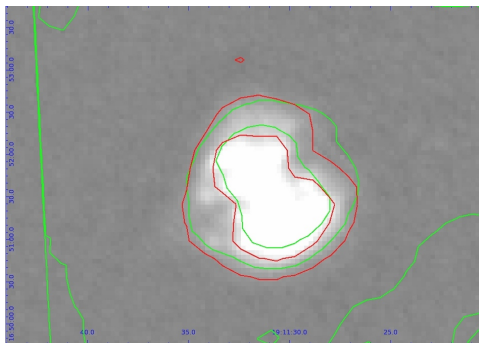
(b) WR31b RGB



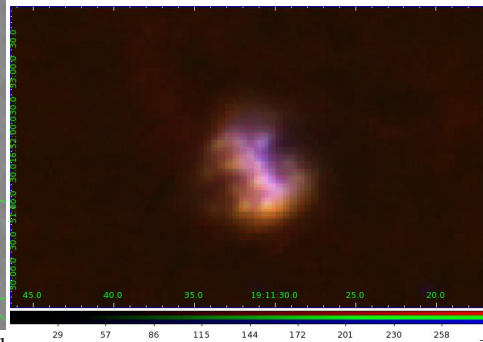
(a) WR75ab: MIPS 24  $\mu\text{m}$  data (green contours) and PACS 70  $\mu\text{m}$  (blue contours)



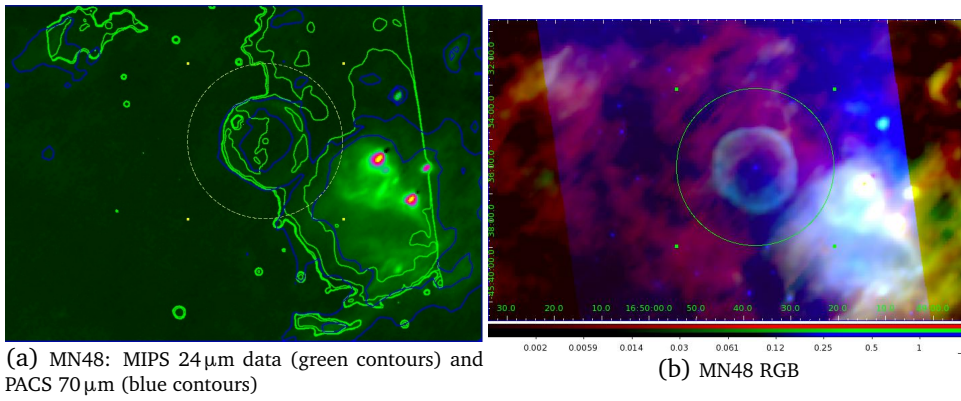
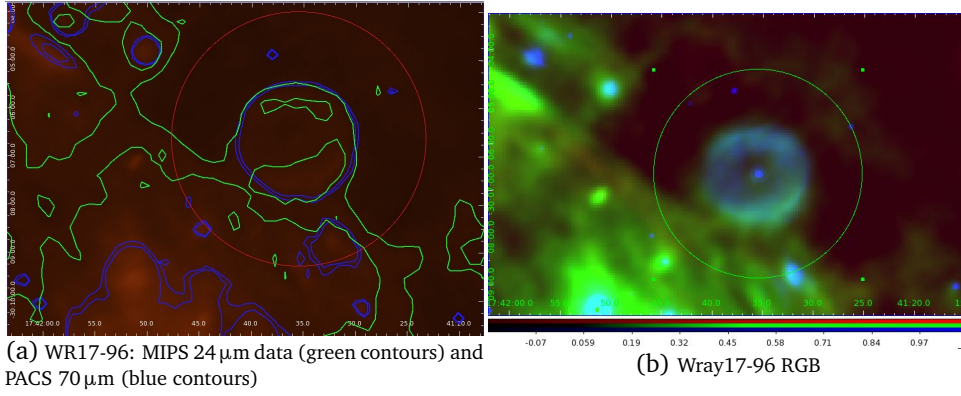
(b) WR75ab RGB



(a) WR124: MIPS 24  $\mu\text{m}$  data (green contours) and PACS 70  $\mu\text{m}$  (red contours)



(b) WR124 RGB



# Appendix B

## The Objects

The contents of this appendix will give a brief description of the objects focused on in this thesis.

### MN27

MN27<sup>1</sup> (see fig.B.1) is a galactic nebulae with a central source discovered with the archival *Spitzer* MIPS-24  $\mu\text{m}$  data.

MN27 exhibits a round shape morphology having a size of  $100\text{arcsec}^2$  (Gvaramadze et al. (2010)). The morphology of the nebula shows unevenness in the brightness but no other significant structure. The central star is clearly evident. The shell was already classified in Wachter et al. (2010) and found it has  $0.7'$  radius and a shell at  $8\mu\text{m}$  with a designated name IRAS 15421-5323. The central source corresponding to MN27 is of WN9h type. WNh stars are luminous Wolf-Rayet (WR) stars of the nitrogen sequence with hydrogen in their spectra.

---

<sup>1</sup>Initials stand for MIPS Nebulae

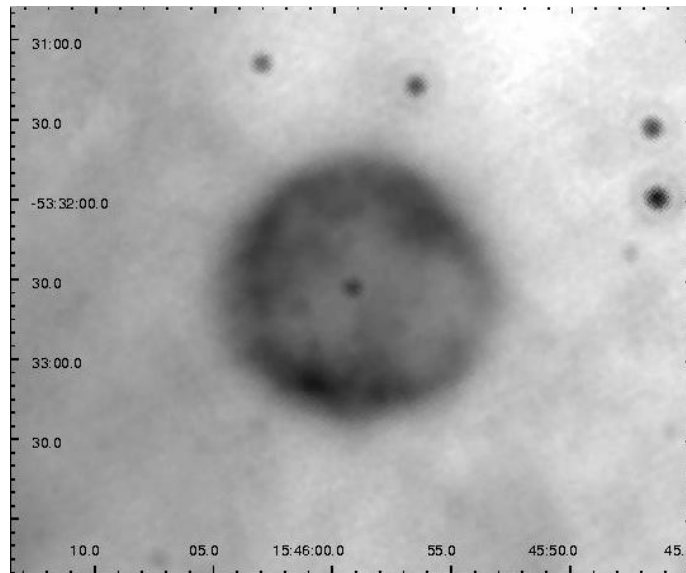


Figure B.1: Spitzer MIPS 24  $\mu\text{m}$  image of MN27. credit:Gvaramadze et al. (2010)

## MN87

MN87 (see fig.B.2), is a galactic nebulae with a central source discovered with the archival *Spitzer* MIPS-24  $\mu\text{m}$  data. It has a size  $60\text{arcsec}^2$  (Gvaramadze et al. (2010)). The source was also mentioned in Wachter et al. (2010) and found to have a  $0.74'$  radius, however no counter part at  $8\mu\text{m}$ . MN87 is also called IRAS 18397-0507. MN87 shows a spherical symmetry with one side being brighter than the opposite probably due to the 'black spot' at the bottom left side of the shell. The 'black spot' could be a foreground star. There exists another spot on the upper right side of the shell that exhibits a small shell of its own. The spot could be another star with a dust ejected forming a circumstellar shell.

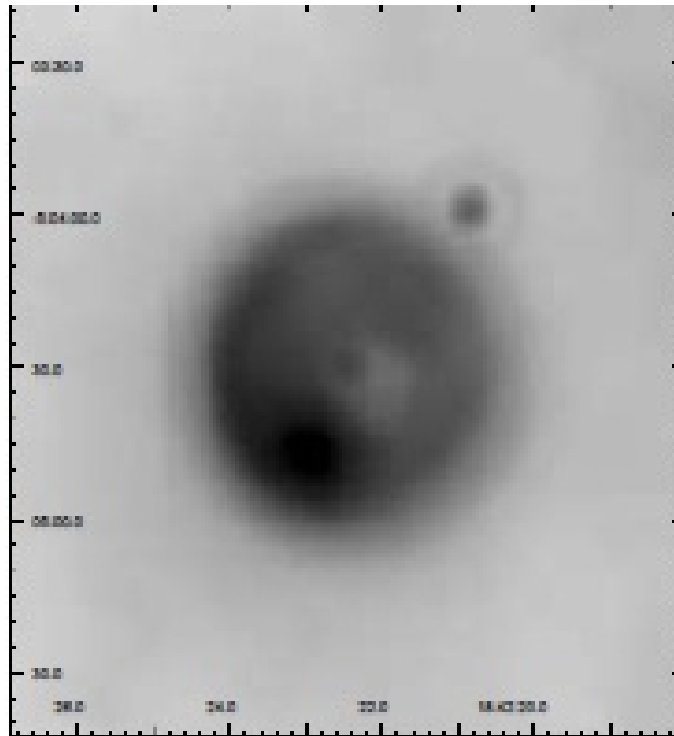


Figure B.2: Spitzer MIPS 24  $\mu\text{m}$  image of MN87. credit:Gvaramadze et al. (2010)

## MN111

MN111 (see fig.B.3) is a galactic nebulae with a central source discovered with the archival *Spitzer* MIPS-24  $\mu\text{m}$  data. It also designated as IRAS 19417+2408. It shows a complex morphology with an irregular rim. The central source might be a big star with detailed dusty patterns around it.

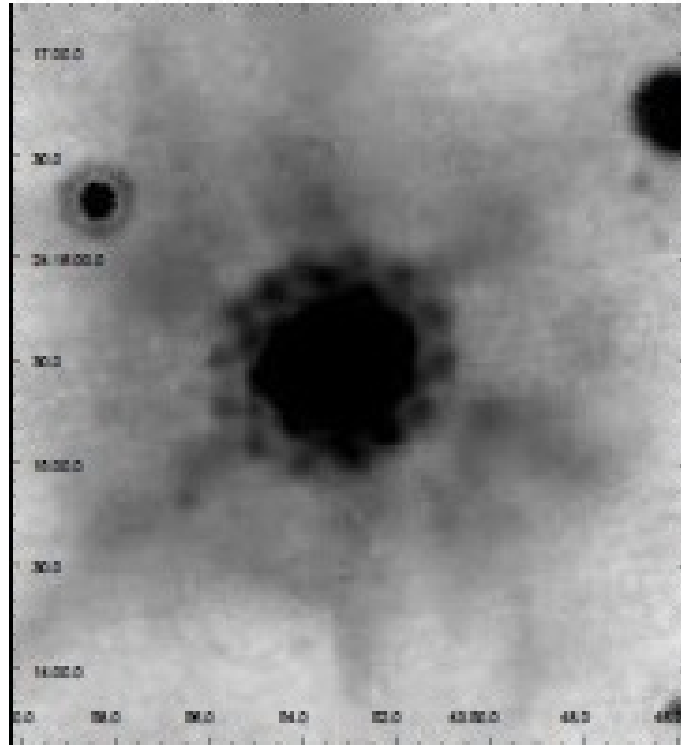


Figure B.3: Spitzer MIPS 24  $\mu\text{m}$  image of MN111. credit: credit:Gvaramadze et al. (2010)

## GAL 024.73+00.69

GAL 024.73 + 00.69 is identified in SIMBAD as a V\* V481 Sct, a variable star of B-class type. It was confirmed as an LBV by Clark et al. (2005) associated by an ejection ring nebula. The shell surrounding GAL 024.73 + 00.69 has a roughly circular morphology with a slight elongation in a direction parallel to the Galactic plane. It shows an innermost small shell and an outermost thick one with what looks to be a star at the bottom left of the shell (see fig). Its shape can be approximated by an ellipse of  $40'' \times 34''$  (Petriella et al. (2011)). On the other hand, Gvaramadze et al. (2010) has found its radius to be  $0.74'$  while Clark et al. (2003) reported a maximal radial extent of  $\approx 1'$  ( $60''$ ). It has a mass-loss rate of  $9.5 \times 10^{-5} M_{\odot}$ , an age of  $\approx 4800$  yr for the nebula and is lying at a distance of 5.2 kpc (Clark et al. (2003)). GAL024.73+00.69 also has a counter part at  $8 \mu\text{m}$ .

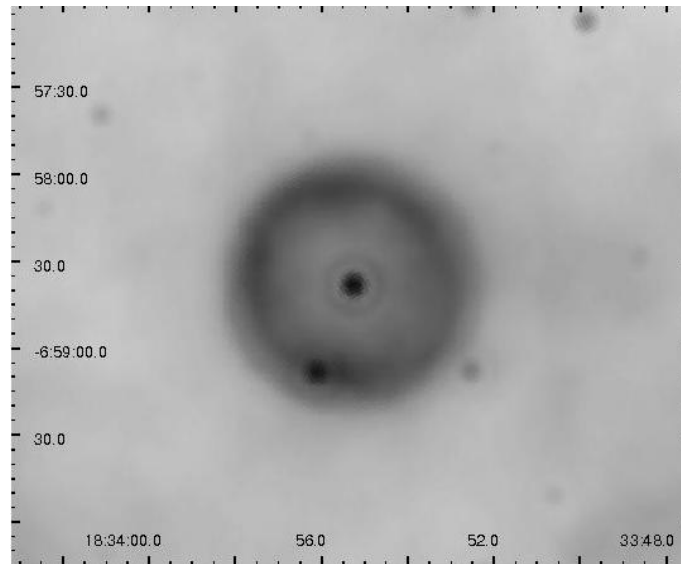


Figure B.4: Spitzer MIPS  $24 \mu\text{m}$  image of GAL024.73+00.69. credit:Gvaramadze et al. (2010)

## WR31a

WR31a is identified by SIMBAD as a Wolf-Rayet star of WN type (with dominant ionized nitrogen in their spectra). The morphology of the shell surrounding WR31a looks dense with an almost perfectly rounded nebular rim. The central source is visible. It is found to be at a distance 8000 pc (van der Hucht (2001)). WR31a is also called IRAS 10520-6010, as well as Hen 3-519.

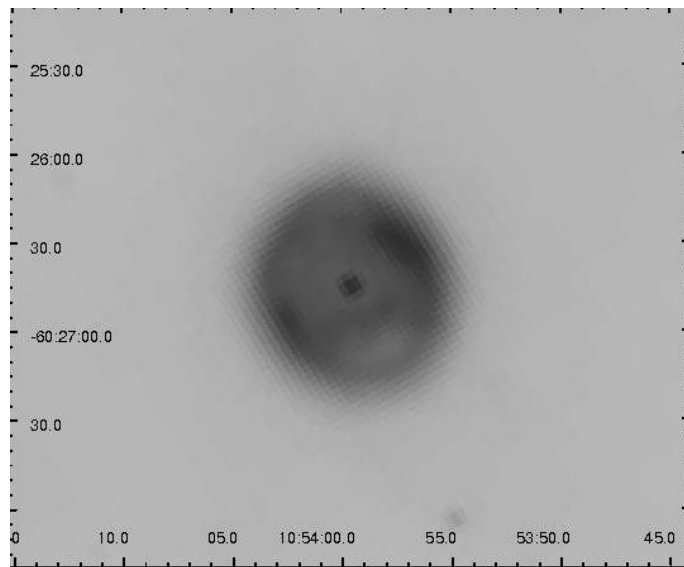


Figure B.5: Spitzer MIPS 24  $\mu$ m image of WR31a. credit:Gvaramadze et al. (2010)

# Bibliography

AAO (2010). Ngc 3372.

Alfaro, E. J., Pérez, E., and Franco, J. (2004). *How Does the Galaxy Work?: A Galactic Tertulia with Don Cox and Ron Reynolds*, volume 315. Springer.

Andersen, A. C. (2007). Dust from agb stars. *arXiv preprint astro-ph/0702618*.

apod (2013). The bubble nebula.

Backman, D. E. and Paresce, F. (1993). Main-sequence stars with circumstellar solid material: the vega phenomenon. *Protostars and planets III*, 1253.

Ballesteros-Paredes, J., Klessen, R., Mac Low, M.-M., and Vazquez-Semadeni, E. (2007). Molecular cloud turbulence and star formation. *Protostars and planets V*, 1:63–80.

Bally, J. and Reipurth, B. (2006). *The birth of stars and planets*. Cambridge University Press.

Beuther, H., Churchwell, E. B., McKee, C. F., and Tan, J. C. (2006). The formation of massive stars. *arXiv preprint astro-ph/0602012*.

Bianchi, S. and Schneider, R. (2007). Dust formation and survival in supernova ejecta. *Monthly Notices of the Royal Astronomical Society*, 378(3):973–982.

Blöcker, T. (1995). Stellar evolution of low and intermediate-mass stars. i. mass loss on the agb and its consequences for stellar evolution. *Astronomy and Astrophysics*, 297:727.

Blondin, J. M. and Lundqvist, P. (1993). Formation of the circumstellar shell around sn 1987a. *The Astrophysical Journal*, 405:337–352.

Bonnell, I. A. and Dobbs, C. L. (2006). Spiral arm triggering of star formation. *Proceedings of the International Astronomical Union*, 2(S237):344–350.

Boulanger, F., Cox, P., and Jones, A. (2000). Course 7: Dust in the interstellar medium. In *Infrared Space Astronomy, Today and Tomorrow*, volume 1, page 251.

- Carey, S., Noriega-Crespo, A., Mizuno, D., Shenoy, S., Paladini, R., Kraemer, K., Price, S., Flagey, N., Ryan, E., Ingalls, J., et al. (2009). Mipsgal: A survey of the inner galactic plane at 24 and 70  $\mu\text{m}$ . *Publications of the Astronomical Society of the Pacific*, 121(875):76–97.
- Cassinelli, J. (1998). Models for the winds and disks around b [e] stars. *ASTROPHYSICS AND SPACE SCIENCE LIBRARY*, 233:177–188.
- Chiosi, C. and Maeder, A. (1986). The evolution of massive stars with mass loss. *Annual Review of Astronomy and Astrophysics*, 24(1):329–375.
- Clark, J., Egan, M., Crowther, P., Mizuno, D., Larionov, V., and Arkharov, A. (2003). Dusty ring nebulae around new candidate luminous blue variables. *Astronomy and Astrophysics*, 412(1):185–198.
- Clark, J., Larionov, V., and Arkharov, A. (2005). On the population of galactic luminous blue variables. *Astronomy and Astrophysics*, 435(1):239–246.
- Clayton, D. D. (1968). *Principles of stellar evolution and nucleosynthesis*. University of Chicago press.
- Clayton, D. D., Amari, S., and Zinner, E. (1998). Dust from supernovae. In *Dust and Molecules in Evolved Stars*, pages 355–374. Springer.
- coolcosmos (2004). Building the spitzer space telescope.
- Dale, D., De Paz, A. G., Gordon, K., Hanson, H., Armus, L., Bendo, G., Bianchi, L., Block, M., Boissier, S., Boselli, A., et al. (2007). An ultraviolet-to-radio broadband spectral atlas of nearby galaxies. *The Astrophysical Journal*, 655(2):863.
- de Avillez, M. A. and Breitschwerdt, D. (2005). Testing global ism models: A detailed comparison of o vi column densities with fuse and copernicus data. *The Astrophysical Journal Letters*, 634(1):L65.
- De Graauw, T., Helmich, F., Phillips, T., Stutzki, J., Caux, E., Whyborn, N., Dieleman, P., Roelfsema, P., Aarts, H., Assendorp, R., et al. (2010). The herschel-heterodyne instrument for the far-infrared (hifi). *Astronomy & Astrophysics*, 518(L. 6):1–7.
- de Wit, W.-J., Oudmaijer, R., and Vink, J. (2014). Dusty blue supergiants: News from high-angular resolution observations. *Advances in Astronomy*, 2014.
- Dole, H., Lagache, G., Puget, J.-L., Caputi, K. I., Fernandez-Conde, N., Floc’h, E. L., Papovich, C., Perez-Gonzalez, P. G., Rieke, G. H., and Blaylock, M. (2006). The cosmic infrared background resolved by spitzer. contributions of mid-infrared galaxies to the far-infrared background. *arXiv preprint astro-ph/0603208*.

- Dorschner, J., Begemann, B., Henning, T., Jaeger, C., and Mutschke, H. (1995). Steps toward interstellar silicate mineralogy. ii. study of mg-fe-silicate glasses of variable composition. *Astronomy and Astrophysics*, 300:503.
- Draine, B. (2003). Interstellar dust grains. *arXiv preprint astro-ph/0304489*.
- Draine, B. and Lee, H. M. (1984). Optical properties of interstellar graphite and silicate grains. *The Astrophysical Journal*, 285:89–108.
- Draine, B. T. (2009). Interstellar dust models and evolutionary implications. *arXiv preprint arXiv:0903.1658*.
- Drew, J. E., Barlow, M., Unruh, Y., Parker, Q., Wesson, R., Pierce, M., Masheder, M., and Phillipps, S. (2004). Discovery of a wo star in the scutumâĂŹcrux arm of the inner galaxy. *Monthly Notices of the Royal Astronomical Society*, 351(1):206–214.
- Dwarkadas, V. V. (2006). Supernova explosions in winds and bubbles, with applications to sn 1987a. *arXiv preprint astro-ph/0612665*.
- Elmegreen, B. G. and Falgarone, E. (1996). A fractal origin for the mass spectrum of interstellar clouds. *The Astrophysical Journal*, 471(2):816.
- esa (2007). Instruments.
- Evans, A. (1993). The dusty universe. *The dusty universe.*, by Evans, A. *Ellis Horwood, New York, NY (USA), 1993, 248 p., ISBN 0-13-221649-3, Price DM 119.70.*, 1.
- Figer, D. F. (1999). The pistol star: A supergiant among its ponderous peers. *Mercury*, 28:32.
- Gail, H.-P and Sedlmayr, E. (2013). *Physics and Chemistry of Circumstellar dust shells*, volume 52. Cambridge University Press.
- Gall, C., Andersen, A. C., and Hjorth, J. (2010). Genesis and evolution of dust in galaxies in the early universe i. modeling dust evolution in starburst galaxies. *arXiv preprint arXiv:1011.3157*.
- Galliano, F., Dwek, E., and Chaniai, P. (2008). Stellar evolutionary effects on the abundances of polycyclic aromatic hydrocarbons and supernova-condensed dust in galaxies. *The Astrophysical Journal*, 672(1):214.
- Garay, G. (2005). Massive and dense cores: the maternities of massive stars. *Proceedings of the International Astronomical Union*, 1(S227):86–91.
- García-Segura, G. and Mac Low, M.-M. (1993). Wind-blown bubbles in circumstellar ejecta. In *Star Formation, Galaxies and the Interstellar Medium: Proceedings of the 4th EIPC Astrophysical Workshop Held at the Elba International Physics Center, Marciana Marina, Elba Island, Italy, June 1-6, 1992*, page 285. Cambridge University Press.

- Garcia-Segura, G. and Mac Low, M.-M. (1995). Wolf-rayet bubbles. ii. gasdynamical simulations. *The Astrophysical Journal*, 455:160.
- Georgy, C., Meynet, G., and Maeder, A. (2010). Effects of anisotropic winds on massive stars evolution. *arXiv preprint arXiv:1011.6581*.
- Goldreich, P. and Kwan, J. (1974). Molecular clouds. *the Astrophysical Journal*, 189:441–454.
- Griffin, M., Abergel, A., Abreu, A., Ade, P., André, P., Augueres, J.-L., Babbedge, T., Bae, Y., Baillie, T., Baluteau, J.-P., et al. (2010). The herschel-spire instrument and its in-flight performance. *arXiv preprint arXiv:1005.5123*.
- Gvaramadze, V., Kniazev, A. Y., and Fabrika, S. (2010). Revealing evolved massive stars with spitzer. *Monthly Notices of the Royal Astronomical Society*, 405(2):1047–1060.
- Haddock, F. (1958). Introduction to radio astronomy. *Proceedings of the IRE*, 46(1):3–12.
- Hallas, T. (2008). Ngc 6888.
- Han, Z., Chen, X., Zhang, F., and Podsiadlowski, P. (2009). Evolution of binary stars and its implications for evolutionary population synthesis. *Proceedings of the International Astronomical Union*, 5(S262):44–47.
- Harper, G. M., Brown, A., and Guinan, E. F. (2008). A new vla-hipparcos distance to betelgeuse and its implications. *The Astronomical Journal*, 135(4):1430.
- Hauser, M. G. and Dwek, E. (2001). The cosmic infrared background: measurements and implications. *arXiv preprint astro-ph/0105539*.
- Heger, A., Langer, N., and Woosley, S. (2000). Presupernova evolution of rotating massive stars. i. numerical method and evolution of the internal stellar structure. *The Astrophysical Journal*, 528(1):368.
- Heitsch, F., Burkert, A., Hartmann, L. W., Slyz, A. D., and Devriendt, J. E. (2005). Formation of structure in molecular clouds: A case study. *The Astrophysical Journal Letters*, 633(2):L113.
- Hildebrand, R. H. (1983). The determination of cloud masses and dust characteristics from submillimetre thermal emission. *Quarterly Journal of the Royal Astronomical Society*, 24:267.
- Höfner, S. (2009). Dust formation and winds around evolved stars: the good, the bad and the ugly cases. *arXiv preprint arXiv:0903.5280*.
- Hoyle, F. and Fowler, W. A. (1960). Nucleosynthesis in supernovae. *The Astrophysical Journal*, 132:565.

- Humphreys, R. M. and Davidson, K. (1994). The luminous blue variables: Astrophysical geysers. *Publications of the Astronomical Society of the Pacific*, pages 1025–1051.
- Ichiro Inutsuka, S. (2012). Oxford journals. <http://ptep.oxfordjournals.org/content/2012/1/01A307.full.pdf+html>.
- Inoue, T. and Fukui, Y. (2013). Formation of massive molecular cloud cores by cloud-cloud collision. *The Astrophysical Journal Letters*, 774(2):L31.
- Jäger, C., Dorschner, J., Mutschke, H., Posch, T., and Henning, T. (2003). Steps toward interstellar silicate mineralogy: Vii. spectral properties and crystallization behaviour of magnesium silicates produced by the sol-gel method. *Astronomy and astrophysics*, 408(1):193–204.
- Jager, C., Mutschke, H., and Henning, T. (1998). Optical properties of carbonaceous dust analogues. *Astronomy and Astrophysics*, 332:291–299.
- Jones, A. and Jones, A. (2002). Temperature-dependent fir/sub-mm dust emissivity indices: some implications for the diffuse ism dust composition. *EAS Publications Series*, 4:37–37.
- Joye, W. et al. (2013). Saoimage ds9. vers. 6.1. 2. *Computer software. Future Directions for Astronomical Image Display*.
- Karttunen, H., KR, P., Oja, H., et al. (2007). *Fundamental astronomy*. Springer.
- Kaufmann III, W. J. (1988). *Universe*.
- Kawaler, S. D. (1988). Angular momentum loss in low-mass stars. *The Astrophysical Journal*, 333:236–247.
- Koike, C., Hasegawa, H., and Manabe, A. (1980). Extinction coefficients of amorphous carbon grains from 2100 Å to 340 μm. *Astrophysics and Space Science*, 67(2):495–502.
- Krugel, E. (2002). *The physics of interstellar dust*. CRC Press.
- Krumholz, M. R. (2006). High mass star formation by gravitational collapse of massive cores. *arXiv preprint astro-ph/0607429*.
- Kwok, S. (2007). *Physics and chemistry of the interstellar medium*. University Science Books.
- Laher, R. R., Gorjian, V., Rebull, L. M., Masci, F. J., Fowler, J. W., Helou, G., Kulkarni, S. R., and Law, N. M. (2012). Aperture photometry tool. *Publications of the Astronomical Society of the Pacific*, 124(917):737–763.
- Lamers, H. J. and Cassinelli, J. P. (1999). *Introduction to stellar winds*. Cambridge University Press.

- Lamers, H. J., Nota, A., Panagia, N., Smith, L. J., and Langer, N. (2001). Chemical composition and origin of nebulae around luminous blue variables. *The Astrophysical Journal*, 551(2):764.
- Langer, N. and Heger, A. (1997). The evolution of surface parameters of rotating massive stars. *arXiv preprint astro-ph/9711338*.
- Larson, R. B. (1981). Turbulence and star formation in molecular clouds. *Monthly Notices of the Royal Astronomical Society*, 194(4):809–826.
- Li, A. and Draine, B. (2001). Infrared emission from interstellar dust. ii. the diffuse interstellar medium. *The Astrophysical Journal*, 554(2):778.
- Lourakis, M. I. (2005). A brief description of the levenberg-marquardt algorithm implemented by levmar. *Foundation of Research and Technology*, 4:1–6.
- Maeder, A. (1998). Relation between stellar evolution and circumstellar processes. In *Astrophysics and space science*, pages 3–14. Springer.
- Maeder, A. and Meynet, G. (2011). Rotating massive stars through the ages, with applications to wr stars, pop iii stars and gamma ray bursts. *arXiv preprint arXiv:1109.6171*.
- Maeder, A., Meynet, G., Hirschi, R., and Ekström, S. (2006). Rotational mixing in massive stars and its many consequences. In *Chemical Abundances and Mixing in Stars in the Milky Way and its Satellites*, pages 308–313. Springer.
- Manual, P. O. (2011). Herschel-hsc-doc-0832. *available from the ESA Herschel Science Centre*.
- Marston, A., Yocum, D., Garcia-Segura, G., and Chu, Y.-H. (1994). A survey of nebulae around galactic wolf-rayet stars in the southern sky, 2. *The Astrophysical Journal Supplement Series*, 95:151–155.
- Martin, C. L. and Arnett, D. (1993). The ring around sn1987a. In *Evolution of Galaxies and their Environment*, volume 1, pages 332–333.
- Massey, P., Plez, B., Levesque, E. M., Olsen, K., Clayton, G. C., and Josselin, E. (2005). The reddening of red supergiants: when smoke gets in your eyes. *The Astrophysical Journal*, 634(2):1286.
- Matsuura, M., Dwek, E., Meixner, M., Otsuka, M., Babler, B., Barlow, M., Roman-Duval, J., Engelbracht, C., Sandstrom, K., Lakićević, M., et al. (2011). Herschel detects a massive dust reservoir in supernova 1987a. *Science*, 333(6047):1258–1261.
- Mauron, N. and Josselin, E. (2010). The mass-loss rates of red supergiants and the de jager prescription. *arXiv preprint arXiv:1010.5369*.
- McKee, C. F. and Tan, J. C. (2002). Massive star formation in 100,000 years from turbulent and pressurized molecular clouds. *nature*, 416(6876):59–61.

- Meikle, W., Mattila, S., Pastorello, A., Gerardy, C., Kotak, R., Sollerman, J., Van Dyk, S., Farrah, D., Filippenko, A., Höflich, P., et al. (2007). A spitzer space telescope study of sn 2003gd: still no direct evidence that core-collapse supernovae are major dust factories. *The Astrophysical Journal*, 665(1):608.
- Mennella, V., Brucato, J., Colangeli, L., Palumbo, P., Rotundi, A., and Bussoletti, E. (1998). Temperature dependence of the absorption coefficient of cosmic analog grains in the wavelength range 20 microns to 2 millimeters. *The Astrophysical Journal*, 496(2):1058.
- Mezzacappa, A. and Fuller, G. M. (2005). *Open Issues in Core Collapse Supernova Theory*, volume 14. World Scientific.
- Morse, J. A., Davidson, K., Bally, J., Ebbets, D., Balick, B., and Frank, A. (1998). Hubble space telescope wide field planetary camera 2 observations of  $\eta$  carinae. *The Astronomical Journal*, 116(5):2443.
- Motte, F., André, P., and Neri, R. (1998). The initial conditions of star formation in the rho ophiuchi main cloud: wide-field millimeter continuum mapping. *Astronomy and Astrophysics*, 336:150–172.
- NASA (2007). *Vy canis majoris*.
- National Astronomical Observatories, C. A. o. S. (2012). Herschel's view of low-mass star formation.
- Nazé, Y., Chu, Y.-H., Points, S. D., Danforth, C. W., Rosado, M., and Chen, C.-H. R. (2001). Interstellar bubbles in two young h ii regions. *The Astronomical Journal*, 122(2):921.
- Norman, C. A. and Ferrara, A. (1996). The turbulent interstellar medium: generalizing to a scale-dependent phase continuum. *arXiv preprint astro-ph/9602146*.
- Nugis, T. and Lamers, H. (2002). The mass-loss rates of wolf-rayet stars explained by optically thick radiation driven wind models. *ASTRONOMY AND ASTROPHYSICS-BERLIN*-, 389(1):162–179.
- Petriella, A., Paron, S., and Giacani, E. (2011). The molecular gas around the luminous blue variable star g24. 73+ 0.69. *arXiv preprint arXiv:1111.6043*.
- Poglitsch, A., Waelkens, C., Geis, N., Feuchtgruber, H., Vandenbussche, B., Rodriguez, L., Krause, O., Renotte, E., Van Hoof, C., Saraceno, P., et al. (2010). The photodetector array camera and spectrometer (pacs) on the herschel space observatory. *arXiv preprint arXiv:1005.1487*.
- Prialnik, D. (2000). *An introduction to the theory of stellar structure and evolution*. Cambridge University Press.

- Renzini, A. (1981). Evolutionary effects of mass loss in low-mass stars. In *Effects of mass loss on stellar evolution*, pages 319–328. Springer.
- Rho, J., Kozasa, T., Reach, W., Smith, J., Rudnick, L., DeLaney, T., Ennis, J., Gomez, H., and Tappe, A. (2008). Freshly formed dust in the cassiopeia a supernova remnant as revealed by the spitzer space telescope. *The Astrophysical Journal*, 673(1):271.
- Rieke, G., Young, E., Engelbracht, C., Kelly, D., Low, F., Haller, E., Beeman, J., Gordon, K., Stansberry, J., Misselt, K., et al. (2004). The multiband imaging photometer for spitzer (mips). *The Astrophysical Journal Supplement Series*, 154(1):25.
- Rouleau, F. and Martin, P. (1991). Shape and clustering effects on the optical properties of amorphous carbon. *The Astrophysical Journal*, 377:526–540.
- Rowan-Robinson, M. (1986). On the nature of interstellar grains and the interpretation of the iras background radiation. *Monthly Notices of the Royal Astronomical Society*, 219(4):737–749.
- Sander, A., Hamann, W.-R., and Todt, H. (2012). The galactic wc stars: Stellar parameters from spectral analyses indicate a new evolutionary sequence. *arXiv preprint arXiv:1201.6354*.
- Sedlmayr, E. (1994). From molecules to grains. In *Molecules in the Stellar Environment*, pages 163–185. Springer.
- Seeds, M. and Backman, D. (2012). *Foundations of astronomy*. Cengage Learning.
- Siegel (2010). M51 in the far infrared.
- Smith, N. (2007). Discovery of a nearby twin of sn 1987a’s nebula around the luminous blue variable hd 168625: Was sk- 69 202 an lbv? *The Astronomical Journal*, 133(3):1034.
- Smith, N. (2010). Circumstellar material around evolved massive stars. *arXiv preprint arXiv:1010.3720*.
- Smith, N., Arnett, W. D., Bally, J., Ginsburg, A., and Filippenko, A. V. (2012). The ring nebula around the blue supergiant sbw1: pre-explosion snapshot of an sn 1987a twin. *Monthly Notices of the Royal Astronomical Society*, page sts418.
- Smith, N., Gehrz, R. D., Hinz, P. M., Hoffmann, W. F., Hora, J. L., Mamajek, E. E., and Meyer, M. R. (2003). Mass and kinetic energy of the homunculus nebula around  $\eta$  carinae. *The Astronomical Journal*, 125(3):1458.
- Smith, N., Gehrz, R. D., and Krautter, J. (1998). The infrared morphology of  $\eta$  carinae. *The Astronomical Journal*, 116(3):1332.

- Smith, N. and Hartigan, P. (2006). Infrared [fe ii] emission from p cygni's nebula: Atomic data, mass, kinematics, and the 1600 ad outburst. *The Astrophysical Journal*, 638(2):1045.
- Smith, N., Humphreys, R. M., Davidson, K., Gehrz, R. D., Schuster, M., and Krautter, J. (2001). The asymmetric nebula surrounding the extreme red supergiant vy canis majoris. *The Astronomical Journal*, 121(2):1111.
- Smith, N. and Owocki, S. P. (2006). On the role of continuum-driven eruptions in the evolution of very massive stars and population iii stars. *The Astrophysical Journal Letters*, 645(1):L45.
- Stock, D. and Barlow, M. (2010). A search for ejecta nebulae around wolf-rayet stars using the shs ha survey. *Monthly Notices of the Royal Astronomical Society*, 409(4):1429–1440.
- van der Hucht, K. A. (2001). The viith catalogue of galactic wolf-rayet stars. *New Astronomy Reviews*, 45(3):135–232.
- Wachter, S., Mauerhan, J. C., Van Dyk, S. D., Hoard, D., Kafka, S., and Morris, P. W. (2010). A hidden population of massive stars with circumstellar shells discovered with the spitzer space telescope. *The Astronomical Journal*, 139(6):2330.
- Weaver, R., McCray, R., Castor, J., Shapiro, P., and Moore, R. (1977). Interstellar bubbles. ii-structure and evolution. *The Astrophysical Journal*, 218:377–395.
- Weis, K., Duschl, W., Bomans, D., Chu, Y.-H., and Joner, M. (1997). The bipolar structure of the lbv nebula around hr carinae. *arXiv preprint astro-ph/9702198*.
- Williams, P., Kidger, M., Van Der Hucht, K., Morris, P. c.-a., Tapia, M., Perinotto, M., Morbidelli, L., Fitzsimmons, A., Anthony, D., Caldwell, J., et al. (2001). Episodic dust formation by hd 192641 (wr 137)–ii. *Monthly Notices of the Royal Astronomical Society*, 324(1):156–166.
- Willson, L. A. (2000). Mass loss from cool stars: impact on the evolution of stars and stellar populations. *Annual Review of Astronomy and Astrophysics*, 38(1):573–611.